Modeling the phenomena of dehydration and flooding of a polymer electrolyte membrane fuel cell

Dietmar Gerteisen *, Timothy Heilmann, Christoph Ziegler

Fraunhofer Institute for Solar Energy Systems, Heidenhofstr. 2, 79110 Freiburg, Germany

ABSTRACT

A one-dimensional, two-phase, transient PEM fuel cell model including gas diffusion layer, cathode catalyst layer and membrane is developed. The electrode is assumed to consist of a network of dispersed Pt/C forming spherically shaped agglomerated zones that are filled with electrolyte. Water is modeled in all three phases: vapor, liquid and dissolved in the ionomer to capture the effect of dehydration of the ionomer as well as flooding of the porous media. The anode is modeled as a sophisticated spatially reduced interface. Motivated by environmental scanning electron microscope (ESEM) images of contact angles for microscopic water droplets on fibers of the gas diffusion layer, we introduce the feature of immobile saturation. A step change of the saturation between the catalyst layer and the gas diffusion layer is modeled based on the assumption of a continuous capillary pressure at the interface. The model is validated against voltammetry experiments under various humidification conditions which all show hysteresis effects in the mass transport limited region. The transient saturation profiles clearly show that insufficient liquid water removal causes pore flooding, which is responsible for the oxygen mass transport limitation at high current density values. The simulated and measured current responses from chronoamperometry experiments are compared and analyzed.

© 2008 Elsevier B.V. All rights reserved.

1. Introduction

It is known that the cathode of a PEM fuel cell, using hydrogen as fuel, is the limiting component for high performance. The slow kinetics of the oxygen reduction reaction (ORR) lead to a strong decrease of the cell voltage in the low current density region. Additionally, mass transport limitations and instability of the cell voltage occur in the high current density region, where typically liquid water blocks the pathway to the active sites. Therefore, accumulation and transport of liquid water is a major factor in the operation of a low-temperature PEM fuel cell.

Water is typically introduced through both anode and cathode gas streams, additionally produced by the ORR at the cathode catalyst layer (CCL) and forced to the CCL by electro-osmotic drag from the anode side. An excess of liquid water in the porous media, namely the catalyst layer and the gas diffusion layer (GDL), blocks a fraction of the open pores. This accumulated water reduces the path available for the transport of gaseous oxygen or forces oxygen to dissolve and diffuse through water to reach the active sites. This phenomenon is called flooding and it is most problematic in the cathode.

Dissolved water in the ionomer is essential for optimal proton conductivity in the catalyst layer (CL) and membrane. The conductivity of the ionomer, which consists of a fluorocarbon polymer backbone with chemically bonded sulfonic acid groups as side chains, is a very strong function of its water content [1]. Dehydration of the ionomer strongly increases the resistance to the proton transport, causing ohmic losses. Additionally, the active area in the CL depends on the amount of dissolved water in the ionomer due to need for a three-phase boundary for the reaction. This means that the catalyst with the carbon support needs good coupling to the protonic phase, which occurs only if the water content is correct. Therefore, increasing the power density of a PEM fuel cell is basically a water management problem. At present, many transport phenomena during fuel cell operation cannot be directly observed or measured. Thus, inverse modeling is a powerful tool to gain qualitative insights into the dynamics of liquid water transport and its effect on fuel cell performance.

Much model development and simulation work has been done in recent years concerning water distribution in a PEM fuel cell to analyze the corresponding loss mechanisms [2–11]. The models differ strongly in the complexity of the applied physics, the examined components and dimensions of the modeling domains. One-dimensional models are widely used for testing new model approaches because the governing equations can be implemented quickly and the computing time required for parameter studies or

* Corresponding author. Tel.: +49 761 4588 5205; fax: +49 761 4588 9000.
E-mail address: dietmar.gerteisen@ise.fraunhofer.de (D. Gerteisen).

time-dependent problems is short [12–17]. One part of the water management investigations are focused on water transport in the membrane forced by diffusion, convection and electro-osmotic drag. Investigations have been made concerning the dependence of the water content distribution on the cell current or its transient behavior while undergoing a load change [18]. Wu et al. [17] developed a 1D, transient PEM fuel cell model to analyze dynamic characteristics corresponding to various changes in working conditions, such as relative humidity or cell voltage. The phenomena of hydration/dehydration is investigated using different membrane types. Overshoots and undershoots are observed, whereas the model does not account for liquid water. Transient analysis of the water content in the membrane was also investigated by Yan et al. [19] with an isothermal, one-phase model. Chen et al. [20] include the effect of membrane swelling in the transient analysis of the water transport in the membrane (vapor and dissolved) and its influence on performance. The influence of liquid water in the CL and GDL on the performance and the interaction of liquid water in the porous media with the dissolved water in the membrane were not considered in these models. With regard to liquid water, Eikerling [21] developed a detailed cathode model focused only on the catalyst layer (GDL and membrane are not considered). He analyzed the impact of the electrode structure and its physical properties like wettability on the liquid water distribution. In doing so, he made the assumption that the electrode consists of a network of agglomerates, similar to [22–25], highlighting the role of a bimodal pore size distribution for the water distribution. The relative proportion of primary and secondary pores and their wetting properties determine the interplay between reaction and transport processes. With strong simplifications, analytical solutions are shown for three distinct states: a dry state, an optimal wetting state and a fully flooded state. Transient analysis was not done. Madhusudana et al. [26] present a dynamic agglomerate model, but neglect the effect of liquid water. Overshoot and undershoot behavior of the current density to voltage step changes are attributed to species transportation in the agglomerate structure.

The influence of the cell geometry concerning e.g. channel or shoulder width/length on the saturation distribution in the porous media was analyzed in two-dimensional or three-dimensional CFD models, among others, by [27,28,3,29,18]. Siegel et al. [29] used an agglomerate approach for the catalyst layer structure in a 2D, two-phase model. They investigated the saturation profile in the porous media along the channel and its effect on the cell performance. Therefore, the blockage of the active area by liquid water (saturation s) is modeled by the factor $(1 - s)$ in the expression for the reaction kinetics. Wang and Wang [18] investigate the fuel cell performance under load changes with a 3D, along-the-channel model. The water content distribution is analyzed in terms of the voltage response. The model accounts also for the catalyst layer, but neglects liquid water transport in the porous media. A three-dimensional analysis of the distribution of reactants and products under the channel and particularly under the rib is done by Berning and Djilali [3]. For simplification, the catalyst layer is assumed to be a spatially non-resolved interface between the membrane and GDL. Maximum saturation values in the cathode GDL of about 10% at a current density of 1.2 A cm^{-2}, located under the rib towards the CL, are predicted by the model. The capillary pressure–saturation relationship $p_c[s]$ is modeled by the Leverett J-function [30], which is the most common approach in two-phase fuel cell models. This approach leads to a strong driving force for the capillary transport of liquid water, resulting in a low saturation level in the case of a fixed saturation of zero at the boundary towards the gas channel. An alternative expression for the capillary pressure–saturation relationship was suggested by Natarajan and Nguyen [27,28], extracted by fitting an empirical function to the measured $p_c[s]$-curve of a

GDL. The corresponding liquid water diffusion obtained with this expression is four orders of magnitude smaller, which means that extremely high saturation gradients would be necessary in order to induce a flux of liquid water [3]. Thus, the simulation results with a 3D cathode model show high saturation levels close to 1. A capillary pressure–saturation relationship was also measured by Acosta et al. [31] and fitted to an empirical function. They distinguish between the imbibition and drainage curve, leading to a saturation level of about 0.11 and 0.5, respectively, for a conventional gas distributor modeled in 2D. Kumbur et al. [32] investigated the effectiveness of the Leverett approach. They discuss the existence of immobile saturation, a threshold below no continuous liquid phase is formed, and compare different approaches for the relative permeability (Wyllie, Corey, Brooks–Corey and Van Genuchten model). They also suggest the existence of a saturation discontinuity between two porous media with different porosities and wettabilities (GDL/MPL), discuss the characteristics of a material with mixed wettability and analyze the influence of contact angles on the saturation distribution. A polynomial fit of the $p_c[s]$-function was made based on experimental pressure curves. Nam and Kaviany [33] had also suggested immobile saturation several years previously. They investigated the tortuosity effect for the case of liquid water present in a GDL and analyzed the enhancement of the saturation level with different material layers of different wettabilities.

A comprehensive one-dimensional transient fuel cell model which accounts for liquid saturation in the GDL and CL, on both the anode and cathode sides, was developed by Ziegler et al. [34]. The model was expanded from the steady-state model of Weber and Newman [35,36] for time-dependent analysis. Both models account for the Schroeder paradox, describing that the membrane water uptake is less when exposed to 100% relative humidity (RH) than liquid water. Ziegler et al. compared their model against potential sweep experiments. Similar sweep experiments, presented in [37], are used to validate a 1D transient model developed by Shah et al. [38]. The model takes into account the agglomerate structure of the catalyst layers, water in the forms of vapor, liquid and dissolved in the ionomer. A feature of this model is the boundary condition for saturation at the interface GDL ↔ channel. The assumption of vanishing saturation was abandoned; instead, a water flux was set. This allows a high saturation level in the case of a low water outflow. To describe the saturation at the interior boundary GDL ↔ CL, a continuous saturation was assumed contrary to the suggestion of a continuous capillary pressure [33,32]. This results in a saturation distribution with a maximum value in the catalyst layer.

This paper presents a transient PEM fuel cell model based on the assumptions of [39], where the GDL, CL and membrane are spatially resolved in 1D with an agglomerate approach for the structure of the CL. Unlike the model of Shah et al. [38], we assume a discontinuity of the saturation due to the continuous capillary pressure and introduce immobile saturation due to the mixed wettability of the GDL structure. The anode is assumed as non-polarizable since hydrogen is used as fuel, therefore the anode only acts as sophisticated interface for the water management. The model is validated with experimental data for current response, impedance and temperature evolution during voltammetry measurements.

2. Model description

The present model is developed to investigate the dynamic transients of a PEMFC in detail. For this purpose, all components which are responsible for a characteristic response with a certain time constant are considered in the model. These are namely the cathode gas diffusion layer (GDL) that suffers flooding in the case of
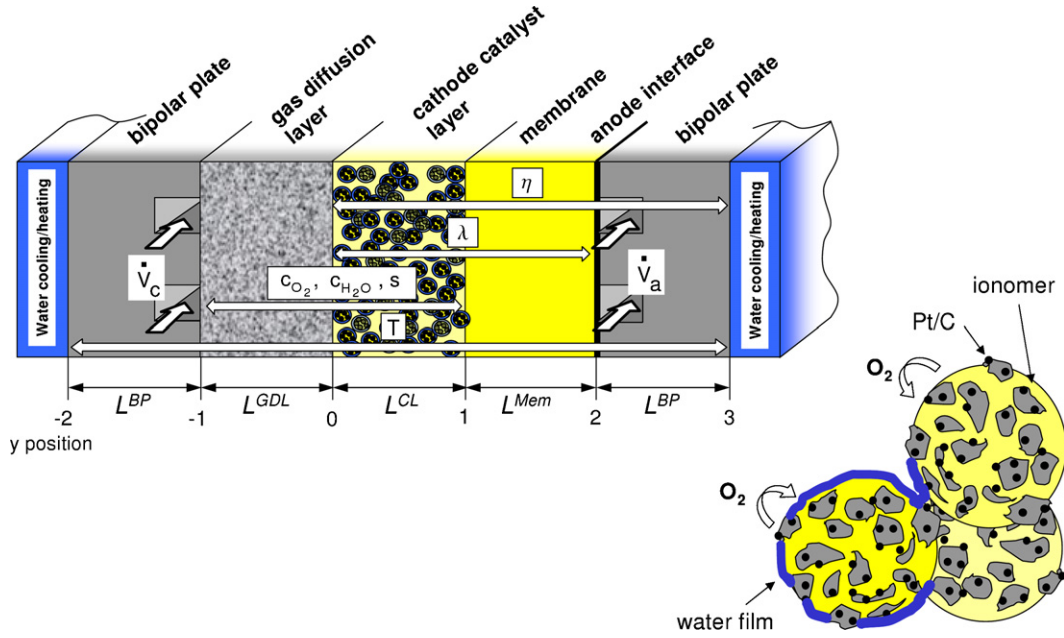
Fig. 1. Schematic diagram of the model domains. The white arrows depict the domains where the solving variables are defined. The catalyst layer (CL) consists of a network of agglomerates where the oxygen reduction reaction take place. When water is present in the CL, it is assumed that the water covers the agglomerates in the form of a thin water film which causes an additional mass transport resistance for the reactant.

insufficient water removal, the cathode catalyst layer (CCL) where the three-phase boundary, the activation overpotential and flooding have a strong influence on the oxygen reduction reaction (ORR) and the membrane with a conductivity that is highly sensitive to its water content and is thus responsible for ohmic losses. Due to the fast kinetics of the hydrogen oxidation and the high hydrogen diffusivity, the polarization losses on the anode side are neglected in the model. We treat the anode as a spatially reduced interface for the boundary conditions. To obtain a realistic temperature distribution within the membrane electrode assembly (MEA), the latter is sandwiched between two model domains that serve for the bipolar plates (BPs).

Altogether, the model consists of five model domains (Ω) which are schematically depicted in Fig. 1. All layers are normalized to a thickness of one for both the numerical applications and better visualization. The real thickness is denoted by L^Ω.

2.1. Considering one agglomerate

Experimental data of Ihonen et al. [40] suggest an agglomerated structure in the catalyst layer with a bimodal pore size distribution. Carbon particles supporting the catalyst (10–20 nm radius) agglomerate to form clusters (agglomerates), which are filled with ionomer acting as a binder. The resulting ionomer-flooded pores with a radius of about 3–10 nm (called primary pores) enable proton conductivity and diffusion of dissolved reactants in the agglomerates. The larger pores between neighboring agglomerates are called secondary pores (10–50 nm). The ORR take place inside the agglomerates where the carbon-supported catalyst forms a three-phase boundary together with the ionomer and the dissolved oxygen. It is assumed that the agglomerates are spherically shaped with a mean radius R_a and homogeneously distributed in the CL. The contact between the agglomerates is sufficient to ensure the free flow of protons and electrons. The tortuosity of the flow path is included in the calculation by a Bruggeman correction. Before the oxygen reaches the catalyst in the agglomerates, it has to dissolve in the ionomer and diffuse to the active sites. In the presence of liquid water in the secondary pores of the CL, water covers the hydrophilic

part of the agglomerates which is the ionomer phase. For mathematical simplification, it is assumed that the water covers the entire agglomerate and forms a thin water film surrounding the agglomerates with a layer thickness d. This implies an additional transport barrier for the oxygen. The oxygen first has to dissolve in water, then diffuse through the water film to reach the ionomer of the agglomerate where the reaction can take place by diffusing to the active sites.

The diffusion of dissolved oxygen is described by Fick's law:

$$j_{O_2}^v[r] = -D_{O_2}^v \, c_{O_2,s}^d \frac{\partial \tilde{c}_{O_2}^d[r]}{\partial r}, \tag{1}$$

where $j_{O_2}^v$ is the oxygen flux in the medium v (v=water agglomerate), $D_{O_2}^v$ is the effective oxygen diffusion coefficient in the medium v and $\tilde{c}_{O_2}^d$ the normalized dissolved oxygen concentration referred to the dissolved oxygen concentration on the water–film surface $c_{O_2,s}^d$ (interface void–water film):

$$\tilde{c}_{O_2}^d[r] = \frac{c_{O_2}^d[r]}{c_{O_2,s}^d}. \tag{2}$$

The distance from the center of the agglomerate is denoted by the spherical coordinate r in brackets. The dissolved oxygen concentration on the water-film surface is calculated from the gaseous oxygen concentration $c_{O_2,s}^g$ above the water film in the secondary pores of the CL using Henry's law:

$$c_{O_2,s}^d = H \, c_{O_2,s}^g, \tag{3}$$

where H is known as the Henry constant [41]. The effective oxygen diffusion coefficient $D_{O_2}^a$ in the agglomerate is calculated by the Bruggeman correlation:

$$D_{O_2}^a = \epsilon_a^{1.5} D_{O_2}^i, \tag{4}$$

where ϵ_a is the fraction of primary pores filled with ionomer and $D_{O_2}^i$ is the diffusion coefficient of dissolved oxygen in the ionomer. The diffusion coefficient of dissolved oxygen in the water film is

used from bulk water diffusion at $60\,^\circ$C (in $m^2\,s^{-1}$) according to Bird, Stewart and Lightfoot [42]:

$$D_{O_2}^w = 4.82 \times 10^{-9}. \tag{5}$$

The oxygen mass balance is given by Eq. (6). Oxygen is not consumed in the water film, whereas the oxygen is reduced in the agglomerate by the ORR described by Tafel kinetics [21,22,24], a simplified approach of the Butler–Volmer kinetics justified at high overvoltages (which is the case at a cell voltage of 900 mV and below):

$$\frac{1}{r^2}\frac{\partial}{\partial r}(r^2 j_{O_2}^v[r]) = \begin{cases} 0 & \text{if } R_a < r \le R_a + d, \\ -k_0 \lambda c_{O_2,s}^d \tilde{c}_{O_2}^d[r]e^{\alpha n F\eta/RT} & \text{if } 0 \le r \le R_a, \end{cases} \tag{6}$$

where k_0 is the reaction rate, α the transfer coefficient, n the number of transfered electrons, R the gas constant and T the local temperature. Following Andreaus et al. [43] and Vielstich et al. [44], both suggesting a dependence of the transfer resistance and reaction rate, respectively, on the ionomer water content and water activity, respectively, we introduce a linear dependency of the ORR rate on the ionomer water content λ (definition see Section 2.3).

The following boundary conditions are used to calculate the current production per agglomerate.

- The concentration of dissolved oxygen on the surface of the water film is related to the local gaseous oxygen concentration in the secondary pores by Henry's law and here assumed as known. The normalized concentration is set to one:

$$\tilde{c}_{O_2}^d[R_a + d] = 1. \tag{7}$$

- A continuous oxygen concentration at the interface water film $[R_a^+] \leftrightarrow$ agglomerate $[R_a^-]$:

$$\tilde{c}_{O_2}^d[R_a^+] = \tilde{c}_{O_2}^d[R_a^-]. \tag{8}$$

- A continuous oxygen flux at the interface water film $[R_a^+] \leftrightarrow$ agglomerate $[R_a^-]$:

$$j_{O_2}^w[R_a^+] = j_{O_2}^a[R_a^-]. \tag{9}$$

- A vanishing oxygen flux in the center of the agglomerate:

$$\frac{\partial \tilde{c}_{O_2}^d[0]}{\partial r} = 0. \tag{10}$$

An analytical solution for the oxygen flux $j_{O_2}[R_a, y]$ at the agglomerate surface ($r = R_a$) as a function of the local overpotential $\eta[y]$, water film thickness $d[y]$ and dissolved oxygen concentration on the surface $c_{O_2,s}^d[y]$ can be found. Using Faraday's law, the current generation of one agglomerate can be calculated by integrating the oxygen flux over the agglomerate surface ∂S:

$$j_{gen}^a[y] = \oint_{\partial S} 4F\vec{j}_{O_2}[R_a, y] \cdot d\vec{A}$$

$$= \frac{4\pi R_a 4F c_{O_2,s}^d[y] D_{O_2}^w D_{O_2}^a (1+d[y])(-1+\Psi\coth[\Psi])}{d[y]D_{O_2}^a \Psi \coth[\Psi] + d[y](D_{O_2}^w - D_{O_2}^a) + D_{O_2}^w}, \tag{11}$$

where

$$\Psi = R_a\sqrt{\frac{k_0 \lambda e^{\alpha n F\eta[y]/RT}}{D_{O_2}^a}} \tag{12}$$

is known as the Thiele modulus [45].

The relationship between the local water-film thickness $d[y]$ and the saturation $s[y]$ of the secondary pores in the CL (which is a solving variable of the model) can be determined by the following calculation.

Considering a unit cell with the volume of one spherical agglomerate ($V_a = \frac{3}{4}\pi R_a^3$) and the surrounding void space (secondary pores) per agglomerate V_p^{dry}, the porosity of the CL can be determined by

$$\epsilon_p^{CL} = \frac{V_p^{dry}}{V_p^{dry} + V_a}. \tag{13}$$

From this it follows:

$$V_p^{dry} = \frac{V_a \epsilon_p^{CL}}{\epsilon_p^{CL} - 1}. \tag{14}$$

The local saturation of the secondary pores in the CL, solved in Eq. (41), is expressed by the ratio of the volume of the thin water film V_{wf} to the secondary pore volume in the dry state:

$$s = \frac{V_{wf}}{V_p^{dry}}, \tag{15}$$

where

$$V_{wf} = \frac{3\pi}{4}((R_a + d)^3 - R_a^3). \tag{16}$$

Inserting Eqs. (14) and (16) into Eq. (15), we obtain a relationship between the water film thickness (surrounding the agglomerates) and the saturation of the CL at the local y-position:

$$d[y] = R_a \left(-1 + \frac{((\epsilon_p^{CL} - 1)^2 (1 + (s[y] - 1)\epsilon_p^{CL}))^{1/3}}{1 - \epsilon_p^{CL}} \right). \tag{17}$$

Combining Eqs. (17) and (11) results in the current generation of an agglomerate $j_{gen}^a[y]$ as a function of the local overpotential, gaseous oxygen concentration and saturation. The analytical expression for $j_{gen}^a[y]$ is used in the following as source/sink terms for the continuity equations of the oxygen concentration and the overpotential in the homogeneous model of the cathode CL that are described in the next sections.

2.2. Activation and ohmic overpotential

The activation overpotential η is the driving force for the ORR and is defined as the deviation of the difference of the electronic potential Φ^e and protonic potential Φ^p from the theoretical open circuit potential $\Delta\Phi^0 = 1.23$ V:

$$\eta = \Delta\Phi^0 - (\Phi^e - \Phi^p). \tag{18}$$

The overall overpotential of a fuel cell is the sum of the activation overpotential in the catalyst layers and the ohmic overpotentials due to finite conductivity of the fuel cell components and contact resistances at the interfaces of the different layers.

Our model takes into account the activation overpotential in the cathode CL, proton migration in the cathode CL and in the membrane. The local change in electric potential in the CL is negligible compared to the change of the protonic potential due to a much higher electric conductivity of the carbon matrix than the proton conductivity of the ionomer and is thus assumed to be constant through the CL. The anode activation overpotential is also neglected due to the fast kinetics of the hydrogen oxidation reaction. The above described ohmic overvoltages of the electrons in the GDLs and BPs as well as the contact resistances are summarized into one model domain, more precisely into the anode bipolar plate (ABP), and modeled with a constant conductivity $\sigma_{contact}$.

Ohm's law is used for the description of the charge flux:

$$j_{p,e} = -\frac{\sigma^\Omega}{L^\Omega} \frac{\partial \eta}{\partial y}, \tag{19}$$

where the superscript Ω stands for the model domain (CL, membrane and ABP). The proton conductivity of the ionomer phase depends on the water content λ and is defined according to Springer et al. [1]:

$$\sigma^\Omega = \begin{cases} \epsilon_i^{1.5} (0.514\lambda - 0.326) e^{1268(1/303 - 1/T)} & \text{if } \Omega = \{L^{CL}, L^{mem}\} \\ \sigma_{contact} & \text{if } \Omega = L^{ABP}. \end{cases} \tag{20}$$

For the ionomer volume fraction in the membrane, a value of $\epsilon_i = 1$ is used and in the catalyst layer $\epsilon_i = \epsilon_i^{CL}$, whereas a Bruggeman correction accounts for the reduction of the pathway for the protons in the CL.

The charge balance equation reads:

$$\frac{\partial j_{p,e}}{\partial y} = \begin{cases} L^{CL} \left(-q_{ORR} - C_{DL} \frac{\partial \eta}{\partial t} \right) & \text{if } \Omega = L^{CL} \\ 0 & \text{if } \Omega = \{L^{mem}, L^{BP2}\}, \end{cases} \tag{21}$$

where C_{DL} is the double layer capacity and q_{ORR} is the current generation per agglomerate j_{agglo} multiplied by the agglomerate density Λ in the CL:

$$q_{ORR} = j_{gen}^a \cdot \Lambda. \tag{22}$$

The agglomerate density is determined by the agglomerate volume and the void space:

$$\Lambda = \frac{1}{V_a + V_p^{dry}} = \frac{3(1 - \epsilon_p^{CL})}{4\pi R_a^3}. \tag{23}$$

2.3. Water content

The water content of the ionomer λ is defined as the ratio of the number of water molecules to the number of charge sites (SO_3^-) in the cathode catalyst layer and in the membrane. The flux of dissolved water in the ionomer j_λ is determined by diffusion and electro-osmotic drag:

$$j_\lambda = \underbrace{-\frac{\varepsilon^{1.5} \rho_i D^i}{EW L^\Omega} \frac{\partial \lambda}{\partial y}}_{diffusion} + \underbrace{\frac{\alpha_{drag}}{F} j_p}_{electro\text{-}osmotic\ drag}, \tag{24}$$

where EW and ρ_i denote the equivalent weight and the density of the ionomer, respectively. The diffusion is forced by the gradient of the dissolved water concentration in terms of the water content. It is assumed that the diffusion coefficient is a function of the water content according to [46]:

$$D_\lambda^i = 2.1 \times 10^{-7} \lambda e^{-(2436/T)}. \tag{25}$$

The electro-osmotic drag coefficient in the second term on the right-hand side is defined as

$$\alpha_{drag} = \frac{2.5\lambda}{22}. \tag{26}$$

The mass conservation equation describes the change in the dissolved water flux:

$$\frac{\partial j_\lambda}{\partial y} = L^\Omega \left(q_{ad} - q_{ur} + \frac{q_{ORR}}{2F} - \frac{\epsilon_i \rho_i}{EW} \frac{\partial \lambda}{\partial t} \right), \tag{27}$$

coupled with phase transition and water generation. The adsorption of water vapor into the ionomer at a water content below the

equilibrium water content λ_{eq} (Eq. (29)) and the desorption in the inverse case follows:

$$q_{ad} = \begin{cases} k_{ads} c_v^* c_v (\lambda_{eq} - \lambda)(1 - s) & \text{if } \lambda \leq \lambda_{eq}, \\ k_{des} \frac{\rho_i}{EW} (1 - s)(\lambda_{eq} - \lambda)(1 - RH) & \text{if } \lambda > \lambda_{eq} \wedge RH \leq 1, \end{cases} \tag{28}$$

where k_{ads} and k_{des} are the adsorption and desorption constants, respectively. The equilibrium water content is a function of the water activity a_w given by Springer et al. [1]:

$$\lambda_{eq}[a_w] = 0.043 + 17.81 a_w - 39.85 a_w^2 + 36.0 a_w^3, \tag{29}$$

where the water activity is equal to the relative humidity RH, calculated by the vapor concentration ($c_v \cdot c_v^*$) (defined in section 2.6) and the saturation pressure $p^{sat}[T]$ for a given temperature:

$$a_w = RH = \frac{(c_v \cdot c_v^*) R T}{p^{sat}[T]} \tag{30}$$

with a saturation pressure (in Pa) according to [1]:

$$\begin{aligned} \log_{10} \left[\frac{p^{sat}[T]}{101325} \right] &= -2.1794 + 0.02953 (T - 273.15) \\ &\quad - 9.1837 \times 10^{-5} (T - 273.15)^2 \\ &\quad + 1.4454 \times 10^{-7} (T - 273.15)^3. \end{aligned} \tag{31}$$

According to the cluster-network model of Weber and Newmann [35,36], we assume a maximum water uptake of the ionomer up to $\lambda_v^{max} = 14$ (given by Eq. (29) at $RH = 100\%$) if the membrane is in contact with water vapor. In the case of liquid water on the membrane surface, ionomer restructuring due to expanding hydrophobic channel occurs, resulting in a maximum water content of $\lambda_l^{max} = 22$. The fraction of expanded channels and thus the water content is a strong function of the existing capillary pressure p_c^i in the ionomer. A relationship is suggested by Weber and Newmann [36]:

$$\lambda[p_c] = \lambda_v^{max} + \frac{1}{2} (\lambda_l^{max} - \lambda_v^{max}) \\ \times \left(1 - \text{erf} \left[\frac{\ln[-1.6 \sigma_w \cos[\Theta_m]] - \ln[10^5 p_c^i]}{0.3 \sqrt{2}} \right] \right), \tag{32}$$

where erf is the error function. The uptake of liquid water by the ionomer if the capillary pressure p_c^{CL} in the secondary pores of the CL (defined in Section 2.4) is higher than in the pore network of the ionomer p_c^i and the liquid water release from the ionomer in the inverse case is given by

$$q_{ur} = \begin{cases} k_u (p_c^i - p_c^{CL}) & \text{if } p_c^i \leq p_c^{CL}, \\ k_r (p_c^i - p_c^{CL}) & \text{if } p_c^i > p_c^{CL}. \end{cases} \tag{33}$$

It is assumed that the ORR produces water in dissolved form $q_{ORR}/2F$. A water accumulation term accounts for the time dependence. The source/sink terms are confined in the CL and vanish in the membrane.

2.4. Saturation

The saturation s is defined in the GDL and CL as the volume of liquid water divided by the volume of secondary pores in the dry state. A high saturation reduces the flow pathway for the oxygen in the porous media that finally results in an increased mass transport resistance. The transport of the liquid water in a porous media is not completely understood but it is well known that the flow in (both hydrophilic and hydrophobic) porous media occurs always from the higher saturation region towards the lower saturation region. The gradient of the capillary pressure is mostly stated as the dominant
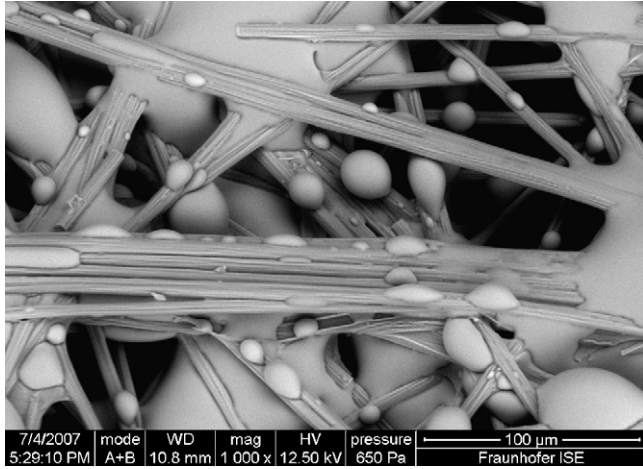
Fig. 2. ESEM image of a Toray TGP-H-090 GDL shows partly hydrophilic regions, leading to the model assumption of immobile saturation.

Fig. 3. A scaled Leverett Function is applied for the capillary pressure–saturation relationship.

force for the water transport. We use Darcy's law for modeling the liquid water transport in porous media:

$$j_s = -\frac{K_{abs}^{\Omega} K_{rel}}{L^{\Omega} \mu} \frac{\partial p_c}{\partial y}, \tag{34}$$

where K_{abs}^{Ω} is the absolute permeability and μ is the water viscosity. The relative permeability K_{rel} and the capillary pressure p_c are sensitive functions of the saturation. There is no consense in the description of the functional variation of the capillary pressure with saturation $p_c[s]$. The most common approaches are the Leverett J-function, the Van Genuchten model [47] and the Brooks-Corey model [48,49] which all have their origin in hydrology (ground water simulation, water/oil flow in unconsolidated rock, etc.). Natarajan et al. [27] suggest a simple exponential approach, agreeing with observed polarization curves.

Environmental scanning electron microscope (ESEM) images of a Toray TGP-H-090 clearly show a mixed wettability of the fiber structure with hydrophobic regions and hydrophilic regions (Fig. 2). This leads to the assumption of immobile saturation (s_{im}) in our model description. Starting from a completely dry GDL, generated liquid water from the CL first fills all the hydrophilic parts of the adjacent GDL pores. If these hydrophilic pores are filled, the local saturation exceeds s_{im} and the water moves by capillary force towards the lower saturation region, where again the hydrophilic pores get filled first. If all hydrophilic regions of the GDL are filled with liquid water then a mobile phase continuity from CL to the gas channel is reached. Below the threshold of s_{im}, water occupying the hydrophilic pores has to evaporate for saturation to decrease further. For the expression of $p_c[s]$ we followed the most widely employed form, the Leverett J-function, but considering the immobile saturation, in the modified form suggested in [33]:

$$p_c^{\Omega} = \sigma_w \cos[\Theta^{\Omega}] \sqrt{\frac{\epsilon_p^{\Omega}}{K_{abs}^{\Omega}}} J^{\Omega}[s], \tag{35}$$

whereby the saturation of the empirical J-function, originally proposed by Udell [30], is replaced by the reduced saturation s_*:

$$s \mapsto s_* = \frac{s - s_{im}}{1 - s_{im}} : \tag{36}$$

$$J^{\Omega}[s] = 1.417\, s_* - 2.12\, s_*^2 + 1.263\, s_*^3. \tag{37}$$

The difference to the original approach can be seen in Fig. 3.

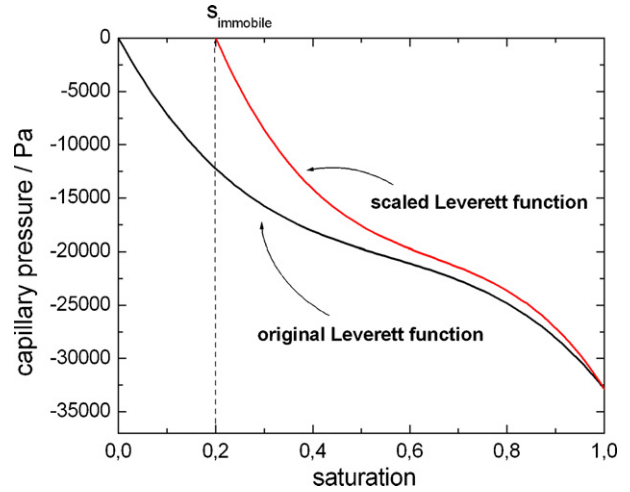We assume a continuous capillary pressure p_c at the interface between CL↔GDL. Due to the different pore size distribution, porosity and wetting properties (contact angle) of the two media (CL/GDL), a continuous capillary pressure results in a discontinuous saturation distribution across the interface [33,32]. Using the chain rule for the derivation of the capillary pressure $\partial p_c / \partial y = (\partial p_c / \partial s)(\partial s / \partial y)$, Darcy's law (Eq. (34)) can be written as a simple diffusion equation for the saturation:

$$j_s = -\frac{D_s^{\Omega}}{L^{\Omega}} \frac{\partial s}{\partial y}, \tag{38}$$

where the diffusion coefficient itself is a function of the saturation:

$$D_s^{\Omega} = \frac{K_{abs}^{\Omega} K_{rel}}{\mu} \frac{\partial p_c^{\Omega}}{\partial s}, \tag{39}$$

with a relative permeability following the cube of saturation:

$$K_{rel} = (s - s_{im})^3. \tag{40}$$

The continuity equation yields:

$$\frac{\epsilon_p^{\Omega}}{\nu_w} \frac{\partial j_s}{\partial y} = L^{\Omega} \left(q_{ec}^{\Omega} + q_{ur} - \frac{\epsilon_p^{\Omega}}{\nu_w} \frac{\partial s}{\partial t} \right), \tag{41}$$

where the interfacial mass-transfer rate between water vapor and liquid water q_{ec}^{Ω} is assumed to be proportional to the saturation in the porous media Ω and proportional to the difference between the existing relative humidity and fully humidified gas:

$$q_{ec} = \begin{cases} k_{eva} \dfrac{RT}{\nu_w} s\, \epsilon_p^{\Omega} c_v^* (RH - 1) & \text{if } RH \leq 1, \\ k_{con} (1-s)\, \epsilon_p^{\Omega} c_v^* c_v (RH - 1) & \text{if } RH > 1. \end{cases} \tag{42}$$

For relative humidity (RH) below 100%, liquid water evaporates (upper term) while for supersaturated gas, water vapor condenses (lower term). The evaporation rate k_{eva} and the condensation rate k_{con} are assumed to be constant [50].

2.5. Oxygen concentration

The oxygen concentration is defined in the CL and GDL. We use simple Fick diffusion for the flux:

$$j_{O_2}^g = -\frac{D_{O_2}^{eff,\Omega} c_{O_2}^{g*}}{L^{\Omega}} \frac{\partial c_{O_2}^g}{\partial y}, \tag{43}$$

where $c_{O_2}^g$ is the normalized gaseous oxygen concentration referred to the oxygen concentration at the boundary to the gas channel

$c_{O_2}^{g*}$, calculated by the ideal gas law with the known oxygen partial pressure p_{O_2} at the cell inlet and the channel temperature T_{ch}:

$$c_{O_2}^{g*} = \frac{p_{O_2}}{R\,T_{ch}}. \tag{44}$$

The values of the GDL porosity published in fuel cell models are prevalently below 0.5 [20,25,13,51,19]. According to the manufacturer, common GDLs have a porosity higher than 0.7 in the uncompressed state [52]. The discrepancy between these two values cannot only be explained by the high compression level in the assembled cell. The answer can be found in the model assumptions. A single-phase model (1, 2 or 3D) does not account for liquid water occupying a part of the void space which results in a lowered effective porosity [53,25]. A two-phase 1D model needs a low porosity as a model parameter to account for in-plane inhomogeneities not only over the entire MEA but also on the scale of a few millimeters as a result of shadowing in the rib↔channel geometry. A simple diffusion simulation in 2D shows that the shadowing by the rib results in minimized apparent porosity for a reduced 1D model.

The effective oxygen diffusivity accounts therefore not only for the porosity (with a realistic value) and the local saturation but also for the spatial reduction to a 1D model with the geometry factor Ξ:

$$D_{O_2}^{eff,\Omega} = \left(\Xi\,\epsilon_p^{\Omega}(1-s)\right)^{1.5} D_{O_2}^g. \tag{45}$$

The temperature and pressure dependence of the free oxygen diffusivity follows the Chapman–Enskog formula [42]:

$$D_{O_2}^g = 3.2 \times 10^{-5} \left(\frac{T}{353}\right)^{1.5} \frac{1}{P}. \tag{46}$$

Taking the reaction into account, the mass balance yields:

$$\frac{\partial j_{O_2}^g}{\partial y} = L^{\Omega}\left(-\frac{q_{ORR}}{4F} - \epsilon_p^{\Omega}(1-s)c_{O_2}^{g*}\frac{\partial c_{O_2}^g}{\partial t}\right). \tag{47}$$

2.6. Water vapor concentration

The governing equation for the vapor flux j_v in the porous media is given by

$$j_v = -\frac{D_v^{eff,\Omega}\,c_v^*}{L^{\Omega}}\frac{\partial c_v}{\partial y}, \tag{48}$$

where c_v is the normalized vapor concentration referred to the inlet vapor concentration c_v^*. The latter is calculated by the saturation pressure p^{sat} (Eq. (31)) for a given humidification temperature T_{DP}^c of the cathode humidifier applying the ideal gas law:

$$c_v^* = \frac{p^{sat}[T_{DP}^c]}{R\,T}. \tag{49}$$

The effective diffusion coefficient $D_v^{eff,\Omega}$ accounts for the porosity of the porous media by the Bruggeman correlation and the clogging of liquid water, which hinders vapor diffusion. The factor Ξ accounts for the shadowing effects of the rib in a real fuel cell (see Section 2.5):

$$D_v^{eff,\Omega} = \left(\Xi\,\epsilon_p^{\Omega}(1-s)\right)^{1.5} D_v^g, \tag{50}$$

where D_v^g is the temperature-dependent diffusivity in a non-porous condition according to Um and Wang [54]:

$$D_v^g = 7.35 \times 10^{-5} \left(\frac{T}{353}\right)^{1.5} \frac{1}{P}. \tag{51}$$

The mass conservation equation can be expressed as

$$\frac{\partial j_v}{\partial y} = L^{\Omega}\left(-q_{ad} - q_{ec}^{\Omega} - \epsilon_p^{\Omega}(1-s)c_v^*\frac{\partial c_v}{\partial t}\right), \tag{52}$$

where adsorption/desorption q_{ad}, evaporation/condensation q_{ec} and a water vapor accumulation term are included.

2.7. Temperature

The heat flux is described by conduction in the solid media and by convection in the form of liquid water, defined in all five layers. Heat convection by the gas flux is neglected. The resulting equation for the heat flux is

$$j_T = -\underbrace{\frac{\kappa^{\Omega}}{L^{\Omega}}\frac{\partial T}{\partial y}}_{conduction} + \underbrace{\epsilon_p^{\Omega} sC_w T j_s}_{convection\ by\ liq.\ water}, \tag{53}$$

where κ^{Ω} is the thermal conductivity of the medium Ω and $C_i = \rho_i c_i$ is the product of the density of the species i and the specific heat capacity. The energy equation reads:

$$\frac{\partial j_T}{\partial y} = L^{\Omega}\left(q_h^{\Omega} - C^{\Omega}\frac{\partial T}{\partial t}\right), \tag{54}$$

where the source term q_h^{Ω} stands for Joule heating, latent heat or reaction and activation loss, depending on the model domain Ω.

In the cathode bipolar plate, Joule heating by the cell current i_{cell} due to the finite electrical conductivity $\sigma_{contact}$ is assumed:

$$q_h^{CBP} = L^{CBP}\frac{i_{cell}^2}{4\,\sigma_{contact}}, \tag{55}$$

where the total electrical and contact resistance (see Section 2.2) is split into components for the cathode BP (25%), the cathode GDL (25%) and the anode BP (50%, including the anode GDL).

Joule heating and latent heat caused by the phase transition in the GDL yields:

$$q_h^{GDL} = L^{GDL}\left(\frac{i_{cell}^2}{4\,\sigma_{contact}} + h_{gl}\,q_{ec}\right). \tag{56}$$

In the CL, the reaction heat of the ORR is the dominant factor, but also latent and ohmic heat is included:

$$q_h^{CL} = L^{CL}\left(\underbrace{(\Delta S T + F\eta)\frac{q_{ORR}}{4F}}_{reaction\ heat} + \underbrace{h_{gl}q_{ec}}_{latent\ heat}\right) - \underbrace{j_p\frac{\partial\eta}{\partial y}}_{ohmic\ heat} \tag{57}$$

Proton migration in the membrane produces heat due to the finite protonic conductivity:

$$q_h^{Mem} = -j_p\frac{\partial\eta}{\partial y}. \tag{58}$$

The heat production in the anode bipolar plate corresponds to that of the cathode BP:

$$q_h^{ABP} = L^{ABP}\frac{i_{cell}^2}{2\,\sigma_{contact}}. \tag{59}$$

The heat capacity C^{Ω} of certain domains Ω are listed below, where the newly introduced subindices (Ti and C) stand for titanium and carbon:

$$\begin{aligned}
&CBP: C^{CBP} = C_{Ti},\\
&GDL: C^{GDL} = \epsilon_p^{GDL} s\,C_w + \epsilon_p^{GDL}(1-s)C_{air} + (1-\epsilon_p^{GDL})C_C,\\
&CL: C^{CL} = \epsilon_p^{CL} s\,C_w + \epsilon_p^{CL}(1-s)C_{air} + (1-\epsilon_p^{CL})C_C,\\
&Mem: C^{mem} = C_{mem}\\
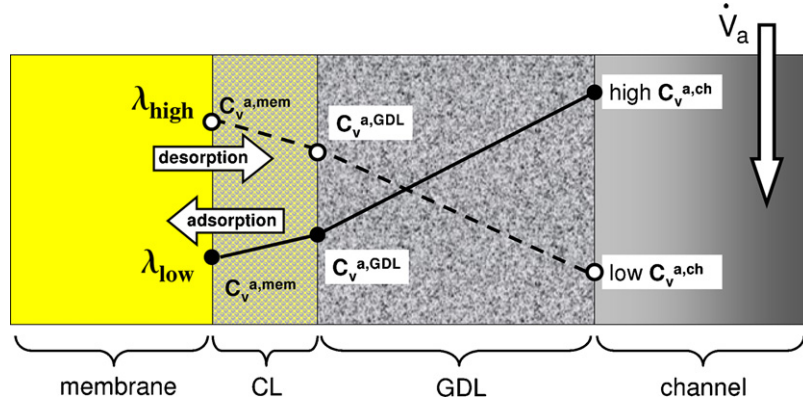&ABP: C^{ABP} = C_{Ti}.
\end{aligned} \tag{60}$$

Fig. 4. The schematic diagram of a spatially resolved anode illustrates the vapor distribution in the cases of desorption (dashed) and adsorption (solid). The reduced anode interface accounts for ad-/desorption and water vapor diffusion, implemented as a lumped boundary condition.

2.8. Boundary conditions

We refer to Fig. 1 for the discussion of the boundary conditions where the solving variables and their area of validity are indicated. If nothing else is stated, we assume continuity in the solving variable and continuous flow at the interior boundaries.

2.8.1. Overpotential η

Since the protons are not allowed to penetrate into the GDL, their flux at this interface ($y = 0$) is taken to be zero:

$$\frac{\partial \eta[0]}{\partial y} = 0. \tag{61}$$

At the boundary of the anode bipolar plate ($y = 3$), the overpotential is set to a value dependent on the simulated cell voltage U:

$$\eta[3] = 1.23V - U - \eta_a, \tag{62}$$

where η_a is the anodic overpotential which is not calculated in the model but can be extracted from the experimental data for reference electrodes [55].

2.8.2. Oxygen concentration $c_{O_2}^g$

The average oxygen concentration at the interface GDL $\leftrightarrow$ flow channel depends strongly on the stoichiometry and flow rate due to oxygen consumption along the channel. To take the air flow rate $\dot{V}_c$ into account, a Cauchy-type boundary condition is chosen:

$$j_{O_2}^g[-1] = \dot{V}_c \, \Omega_{O_2}^c \, c_{O_2}^{g*} \, (1 - c_{O_2}^g). \tag{63}$$

It gives a relationship between the air flow rate, the deviation of the normalized oxygen concentration from 100% and a specific oxygen transfer coefficient $\Omega_{O_2}^c$, chosen large enough that $c_{O_2}^g$ never falls below 90%, even for a high load (which is realistic for small test fuel cells).

We assume that the membrane is an impermeable barrier for gaseous oxygen which implies zero flux at $y = 1$:

$$\frac{\partial c_{O_2}^g[1]}{\partial y} = 0. \tag{64}$$

2.8.3. Water vapor concentration c_v

The flux boundary condition for the water vapor concentration is defined similarly to the oxygen concentration described above:

$$j_v[-1] = \dot{V}_c \, \Omega_v^c \, c_v^* \, (1 - c_v), \tag{65}$$

where Ω_v^c is the specific water vapor transfer coefficient at the interface GDL $\leftrightarrow$ channel.

As for oxygen, the membrane is also impermeable for the water vapor:

$$\frac{\partial c_v[1]}{\partial y} = 0. \tag{66}$$

2.8.4. Water content λ

Since dissolved water, in terms of λ, has no transport mechanism in the gas diffusion layer, its flux is taken to be zero at the interface between CL and GDL:

$$\frac{\partial \lambda[0]}{\partial y} = 0. \tag{67}$$

The boundary condition for the water content on the anode side is extremely complex and needs a detailed explanation.

In consideration of the fact that on the anode side, neither the catalyst layer nor the gas diffusion layer is spatially resolved, the relevant transport mechanism and phase transitions therein have to be reduced to an interface with a sophisticated boundary condition. For better understanding of the layer reduction to a simplified interface, an illustration of the local variables is given in Fig. 4. In order to allow dehydration of the ionomer on the anode side we do not fix the water content λ to a certain value but use a Cauchy-type boundary condition as follows.

We calculate the equilibrium water vapor partial pressure at the membrane surface $p_v^{a,mem}$ for a given water content at the anode interface ($\lambda[2]$) by means of the inverse function $\lambda_{eq}^{-1}[a_w]$ of Eq. (29) and the saturation pressure $p^{sat}[T]$:

$$p_v^{a,mem} = p^{sat}[T] \, \lambda_{eq}^{-1}[a_w]. \tag{68}$$

The vapor pressure can be converted by means of the ideal gas law to a vapor concentration:

$$c_v^{a,mem} = \frac{p_v^{a,mem}}{RT}. \tag{69}$$

Neglecting vapor diffusion in the catalyst layer, we use the CL thickness for a simple adsorption/desorption region, where a linear dependence of the adsorption/desorption process on the difference between the equilibrium vapor concentration $c_v^{a,mem}$ at the membrane surface and the existing vapor concentration $c_v^{a,GDL}$ between CL and GDL is assumed. The vapor flux at the boundary $CL \leftrightarrow GDL$ can be written as

$$j_{ad}^a = L^{CL} \, k_{ad}^a (c_v^{a,GDL} - c_v^{a,mem}), \tag{70}$$

where L^{CL} is the anode CL thickness and k_{ad}^{a} the adsorption/desorption rate, expressed as

$$k_{ad}^{a} = \begin{cases} 5 \times 10^{-5} \, k_{des} & \text{if } c_{v}^{a,mem} > c_{v}^{a,GDL}, \\ 5 \times 10^{-5} \, k_{ads} & \text{if } c_{v}^{a,mem} \leq c_{v}^{a,GDL}. \end{cases} \quad (71)$$

The vapor diffusion in the GDL, forced by the vapor concentration gradient, is written as

$$j_{diff}^{a} = -D_{v}^{eff,\Omega} \frac{(c_{v}^{a,cha} - c_{v}^{a,mem})}{L_{GDL}}, \quad (72)$$

where $D_{v}^{eff,\Omega}$ is the effective vapor diffusion coefficient and $c_{v}^{a,cha}$ is the vapor concentration in the anode channel.

The condition of continuity of both fluxes, provided that there is no phase change in the GDL, results in

$$j_{ad}^{a} = j_{diff}^{a} = \frac{-D_{v}^{g} (c_{v}^{a,mem} - c_{v}^{a,cha}) L^{CL} k_{ad}^{a}}{D_{v}^{g} + L^{CL} k_{ad}^{a} L^{GDL}}. \quad (73)$$

As a boundary condition for the water content on the anode side, we couple the dissolved water flux with the derived vapor flux:

$$j_{\lambda} = \frac{-D_{v}^{g} (c_{v}^{a,mem} - c_{v}^{a,cha}) L^{CL} k_{ad}^{a}}{D_{v}^{g} + L^{CL} k_{ad}^{a} L^{GDL}} - \frac{\dot{V}_{a}}{v_{g}} \Omega_{w}^{a} (\lambda - 14) \theta[\lambda - 14], \quad (74)$$

where the last term on the right-hand side accounts for the case of high water content ($\lambda > 14$) when the ionomer releases liquid water, carried out by the hydrogen gas stream. A high value of $\Omega_{w}^{a} = 600 \, m^{-2}$ is chosen for fast water release and $\theta[x]$ is the Heavyside function (equal to 1 for $x > 0$ and 0 elsewhere).

2.8.5. Saturation s

The accumulation and removal of liquid water on top of the GDL (towards the channel) is a complicated process. Water forms droplets which are blown out by the convective force of the gas stream. The greater the flow velocity in the channel, the more efficient the removal of liquid water. Such a sophisticated dynamic approach can hardly be reproduced in a 1D model. As a strongly simplified approach, we implemented an outflow condition for the saturation as a quadratic function of the difference between the saturation itself and the immobile saturation s_{im}:

$$j_{s}[-1] = \begin{cases} -\frac{\dot{V}_{c}}{v_{g}} \Omega_{s}^{c} (s - s_{im})^{2} & \text{if } s \geq s_{im}, \\ 0 & \text{if } s < s_{im}, \end{cases} \quad (75)$$

where the flow rate has a linear influence on the liquid water flux.

The interior boundary of the saturation differs from the other solving variables by having a discontinuity in its distribution. Continuous capillary pressure is assumed at the interface GDL $\leftrightarrow$ CL:

$$p_{c}^{GDL}[0] = p_{c}^{CL}[0], \quad (76)$$

which is, in our opinion, the physically realistic boundary condition. This results in a saturation discontinuity at the interface (in the case of different structural properties and wettabilities such as porosities and contact angles) but with a continuous liquid water flux:

$$j_{s}^{GDL}[0] = j_{s}^{CL}[0]. \quad (77)$$

A zero-flux boundary for liquid water is assumed at the interface CL $\leftrightarrow$ membrane:

$$\frac{\partial s[1]}{\partial y} = 0. \quad (78)$$

2.8.6. Temperature T

With regard to our water-cooled fuel cell (which provided the measured data we use for the model validation), we use Cauchy boundary conditions that consider a linear dependence of the heat removal on the difference between the temperature at the outer side of the BPs and the cooling-water temperature:

$$j_{T}[-2] = j_{T}[3] = \Omega_{T} (T - T_{coolant}), \quad (79)$$

where Ω_{T} is the heat transfer coefficient dependent on the coolant flow rate.

2.9. Impedance

The membrane impedance (Z) is calculated by an integral over the inverse membrane conductivity (Eq. (20)) along the membrane thickness:

$$Z = \int_{1}^{2} \frac{L^{mem}}{\sigma^{mem}} dy. \quad (80)$$

2.10. Numerical details

The governing equations are solved using *COMSOL Multiphysics* TM, a commercial software package based on finite element methods. A Direct Linear System Solver (UMFPACK) and quadratic Lagrange polynomials as test functions are used. The solver is allowed to take free time steps. The five model domains are discretized with a non-uniform grid of 265 elements whereas the CL and the regions near the interfaces between the domains are refined with smaller elements.

3. Experimental

The experiments were made with a small test fuel cell (geometric area of $1 \, cm^{2}$) in a test bench that are both described in detail in Gerteisen [55]. Note that, due to the reference electrode configuration used, we are able to separate the anode overvoltage from the remaining cell losses, which is important for the validation of a fuel cell model where the anode losses are neglected. An untreated gas diffusion layer of type TORAY®TGP-H-090 was utilized. A GORE TM PRIMEA® Series 5510 MEA with *Pt* catalyst (loading anode/cathode: 0.4 mg cm^{-2}) and a membrane thickness of 35 μm was used. For analyzing water transport, flooding effects and membrane dehydration, dynamic measurements were performed that give a good insight into the processes that occur. We used voltammetry and chronoamperometry experiments. To prove the validity of the model, we investigated the current response of the cell for three different humidification conditions of the inlet gases, denoted as case (1): $air_{dry}/H_{2_{dry}}$, case (2): $air_{dry}/H_{2_{hum}}$ and case (3): $air_{hum}/H_{2_{hum}}$. Detailed operating conditions such as the dew point temperature of the inlet gases and flow rates are summarized in Table 1.

Voltammetry experiments were conducted in the voltage range between 900 mV and 60 mV with a scan rate of 10 mV s^{-1}.

Table 1
Operating conditions in the voltammetry experiments

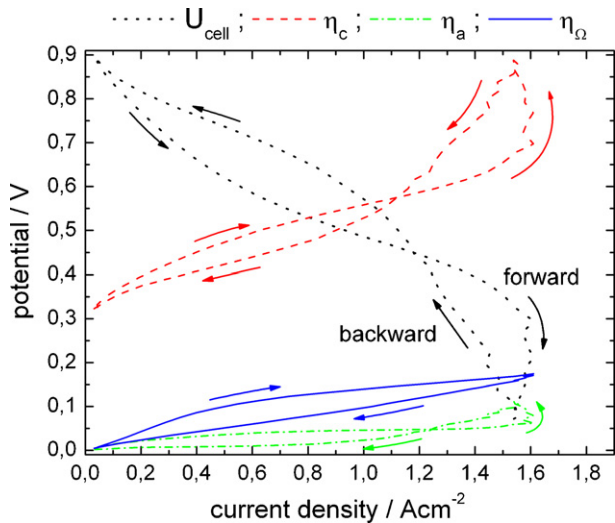|	Case	Cathode	Anode
Dew point temperature of inlet gases: T_{DP}^{Ω}/K	(1)	Dry	Dry
	(2)	Dry	309
	(3)	309	309
Coolant temperature: $T_{coolant}$/K	(1)–(3)	313	313
Gas flow rate: $\dot{V}_{\Omega}$/ml min^{-1}	(1)–(3)	100 (air)	50 (H$_2$)

Fig. 5. A typical voltammetry measurement that shows MEA dehydration at high cell voltage and flooding in the limiting current density region which results in two hysteresis loop like a "eight". By means of reference electrode measurements the overall cell loss can be separated into cathode, anode and ohmic losses.

Several sweeps were applied sequentially to reach and ensure reproducibility of the dynamic characteristic of the I–U curve. The cell impedance at 10 kHz was recorded during all experiments. The temperature was measured with a thermocouple in the anode plate 1 mm above the flow field .

Chronoamperometry is a measurement technique in which the cell voltage is switched between two values, and the resulting cell current response is monitored as a function of time. The characteristic of the current response and cell impedance, triggered by a voltage change from

- step (1): 600–300 mV,
- step (2): 700–400 mV,
- step (3): 800–500 mV and vice versa, was investigated.

4. Results and discussion

4.1. Voltammetry experiments

Voltammetry experiments were used to validate the developed model with measured data. Therefore, we briefly discuss the experimental results to establish an understanding of the measured
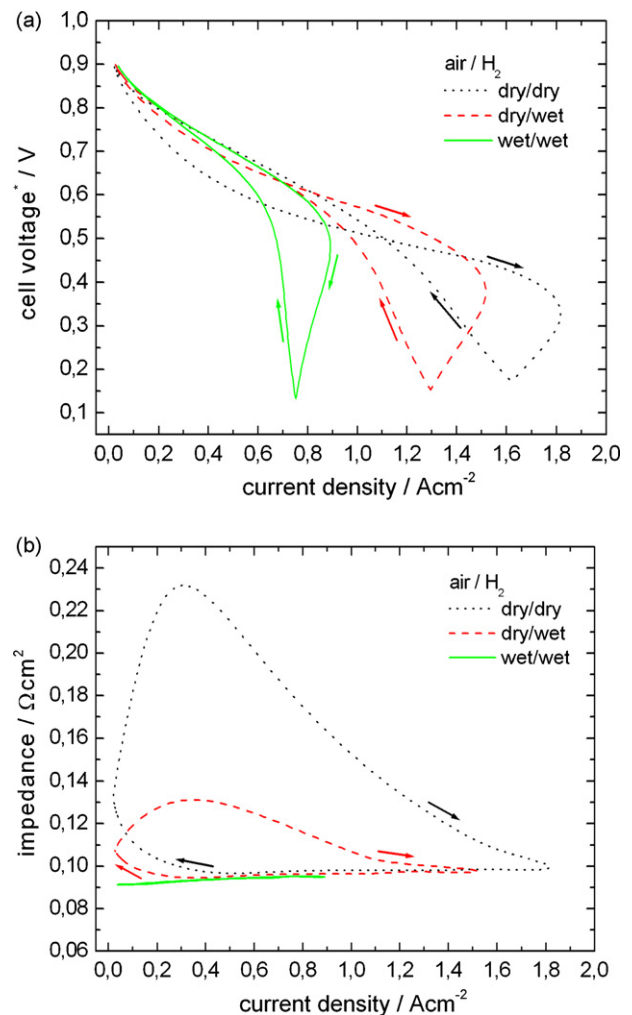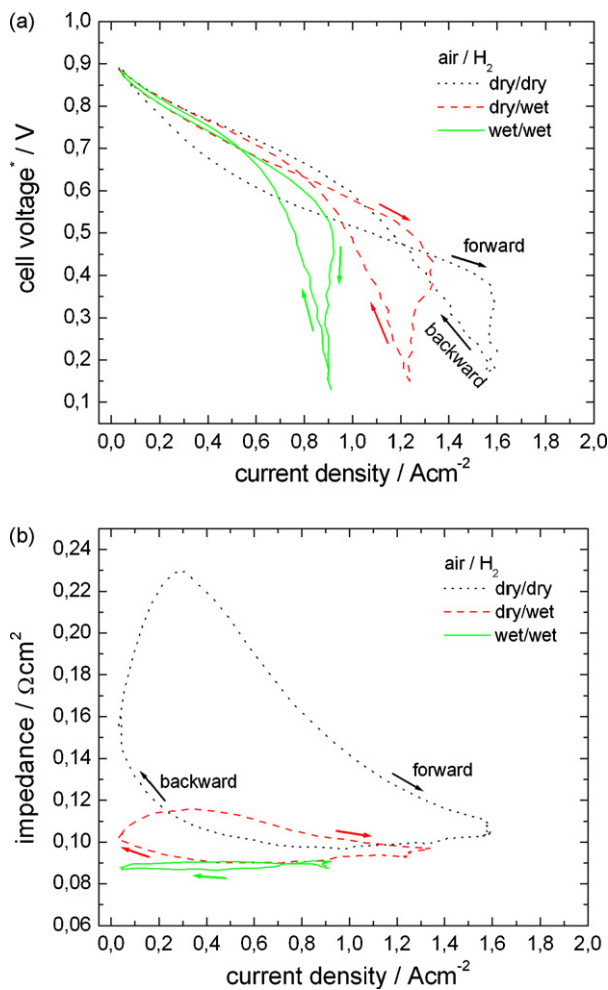

Fig. 6. Voltammetry experiments with a scan rate of $10\,mVs^{-1}$ were conducted to validate the developed model. (a) Voltammetry experiments conducted under different humidification conditions show strong hysteresis effects. (b) Measured cell impedances show a large dynamic range in dehydration and humidification of the ionomer.

Fig. 7. The simulated polarization curves and impedance characteristics show a similar influence on the humidification conditions as the measurement. (a) The simulated current–voltage characteristic show strong hysteresis effects with about the same limiting current density as the measurement. (b) The increase of the impedance lies in the same range as the experiment.

dynamic effects. As an example, Fig. 5 shows the cell voltage, separated into cathode, anode and ohmic overvoltage during a dynamic voltammetry experiment (forward and backward sweep) for dry operating conditions. It can be seen that the anode overvoltage has minor impact on the overall cell loss but is not completely negligible, which has to be in mind for the validation. Fig. 6(a) shows the polarization curves of voltammetry experiments for three different humidification conditions (cases (1)–(3)). The corresponding cell impedance is depicted in Fig. 6(b). The forward (900–60 mV) and the backward sweeps (60–900 mV) are labeled by arrows. For comparison with the simulation results, the cell voltage is corrected by the anode losses and denoted by the superscript *. The polarization characteristic is strongly influenced by the humidification conditions in such a way that under completely dry conditions (case (1)), the highest limiting current density is reached at the expense of ionomer dehydration at low current density. Fig. 6(b) shows for case (1) that the impedance increases throughout a backward sweep and further increases in the forward sweep up to a maximum value of approximately 230 $m\Omega cm^2$; thereafter the water production is sufficient to humidify the ionomer itself. The increasing impedance in the low current density range is responsible for the hysteresis effect in the polarization curve in that region. The observed lower limiting current density in the case of higher humidification (cases (2) and (3)), leads to a decline from $1.6\,A\,cm^{-2}$ to $1.3\,A\,cm^{-2}$ and $0.9\,A\,cm^{-2}$, respectively, indicating higher oxygen transport limitations due to increased flooding phenomenon. The saturation level during the voltammetry experiment is strongly time-dependent and causes hysteresis loops in the high current density region in all three cases. The dehydration of the ionomer is considerably reduced in case (2), compared to the completely dry conditions in case (1), and almost prevented for case (3).

4.2. Model validation

The simulation results for the three different sets of operating conditions are shown in Fig. 7. The values of the model parameters used for the simulation are listed in the parameter list in Section 6 and are also used in simulations that are discussed in the next sections.

Under all three different operating conditions, the model predicts the same current–voltage characteristics as the measurements, as shown in Fig. 7(a). In all three cases the simulations show hysteresis effects in the high current density region with about the same limiting current density. In case (1), the pronounced hysteresis loop in the low current density region is observed too. The time-dependent behavior of the simulated impedance (Fig. 7(b)) is in good agreement with the measurement. In case (1) with completely dry conditions, the simulated impedance shows also a strong variation with the same maximum value as the experiment. In case (2), the dehydration of the ionomer is less pronounced and the impedance in case (3) is nearly constant, as found in the measured data.

A comparison of the temperature change throughout a sweep experiment is made in Fig. 8. On the left-hand side, the measured temperature is shown for the three different sets of humidification conditions. It is evident that the cell cooling is not sufficient to keep the temperature constant during a potential sweep. The high current density in case (1) is responsible for a temperature rise of 3.5 K from 313.5 K to 317 K. For comparison, we analyze the simulated temperature at the interior boundary between the anode plate and the anode interface $T[2]$, depicted in Fig. 8(b). The simulated temperature shows the same qualitative characteristic as the measurement. The temperature variation falls in the same range of 3.5 K for case (1), 3 K for case (2) and 2 K for case (3).
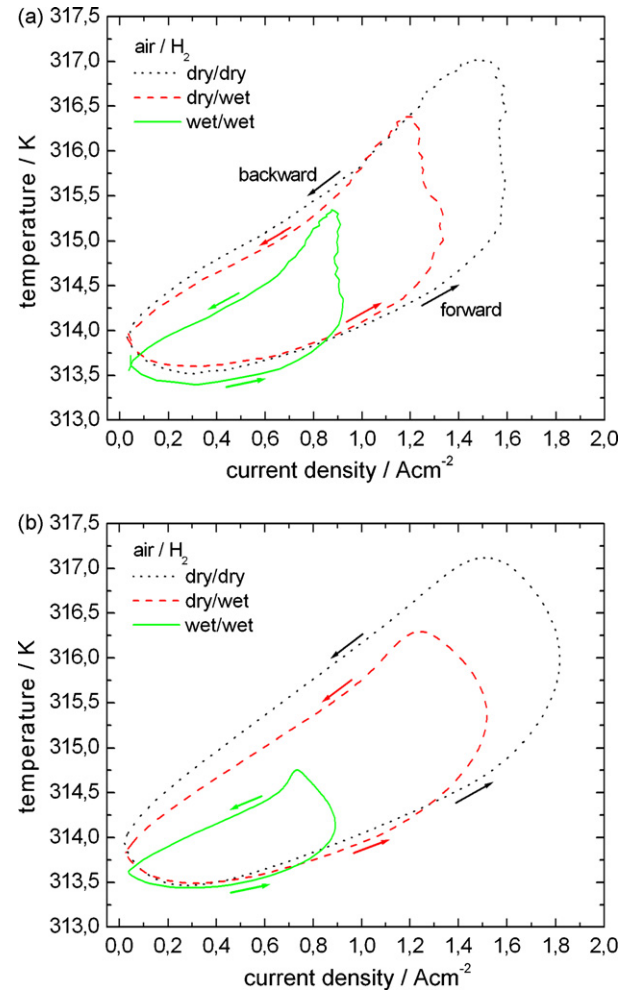

Fig. 8. A qualitative agreement between the measured temperature in the anode plate and the simulated temperature is achieved. (a) The temperature of the cell increases up to 2–3.5 K depending on the load. (b) The non-isothermal model predicts qualitatively the same dynamics for the cell temperature.

4.3. Analysis of the solving variables

In this subsection, we discuss the origin of the hysteresis effects in detail on the basis of the profiles of certain solving variables. The following plots show snapshots of some profiles either at 0.7 V or 0.4 V during a simulated voltammetry experiment.

For the analysis of the hysteresis loop in the low current density region, which is most pronounced in case (1), we refer to the water content λ at 0.7 V. In Fig. 9(a), a large difference in the water content between forward and backward sweeps is present in cases (1) and (2). The low water content in the forward mode results in a high ohmic drop in the membrane which finally results in a minimized activation overpotential in the cathode CL for the ORR (Fig. 9(b)). In addition, the lower water content reduces the area of the three-phase boundary zone and therefore decelerates the reaction kinetics (see Eq. (6)). The fact that oxygen transport limitation is not responsible for the lowered current generation, which might be possible in the case of different saturation levels, is shown in Fig. 10. In the forward mode, more oxygen is available for the ORR than in the backward mode. Fig. 11(b) shows that the relative humidity in the CL remains at nearly 100% except for forward sweeps of cases (1) and (2) where dry cathode inlet gases are used. The difference of saturation between forward and backward sweeps at 0.4 V is depicted in Fig. 11(a). The saturation
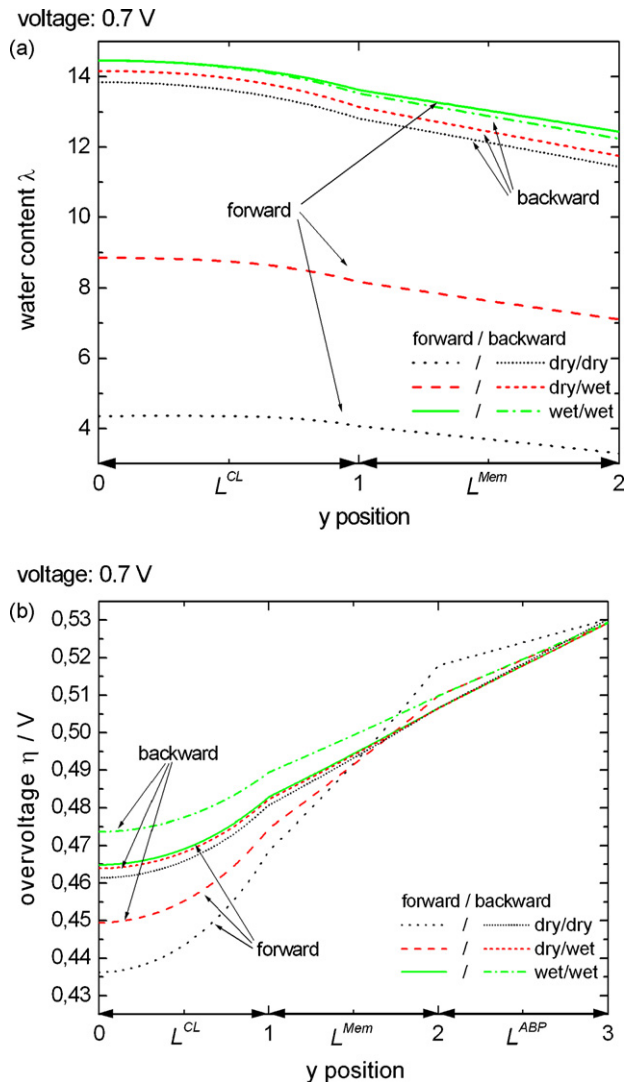
Fig. 10. A comparison of the profiles of the normalized oxygen concentration (0.7 V) during a forward and a backward sweep. Higher transport limitations are observed in the backward sweep.

Fig. 9. A snapshot of the profiles of the water content and the overpotential between forward and backward sweeps at 0.7 V is given. (a) A comparison of the water content profile shows a strong dehydration of the ionomer in cases (1) and (2). (b) The steep ohmic drop in the membrane in case (1) leads to a minimized activation overpotential in the CL, resulting in low current generation.

level in a backward sweep is always above its level in the forward mode. The largest difference is observed in case (1), where the saturation differs up to 20% in the GDL. The saturation level of the GDL in our simulations is uncommonly high compared to previous publications [51,3,33,8,10,11]. The reason for it is based firstly on the assumption of an existing immobile saturation of $s_{im} = 0.2$, and secondly in the choice of Cauchy boundary conditions at the interface GDL $\leftrightarrow$ channel. The most common assumption for the boundary condition is vanishing saturation at the interface towards the channel. The high capillary force in the presence of a large saturation gradient, predicted by the Leverett J-function, results in a fast liquid water outflow. This implies a small curvature of the saturation profile and finally a low saturation level in the GDL in the case of a Dirichlet boundary condition: $s = 0$ at the interface GDL $\leftrightarrow$ channel. Wang et al. [56] predicts a maximum saturation level of only about 6.3% at a current density of about 1.4 A cm^{-2} in the case of the commonly made assumptions. Such a low saturation level would not lead to mass transport limitations at a current density of about 1.0 A cm^{-2} (using realistic values of the GDL porosity), that are clearly observed in our experiments.
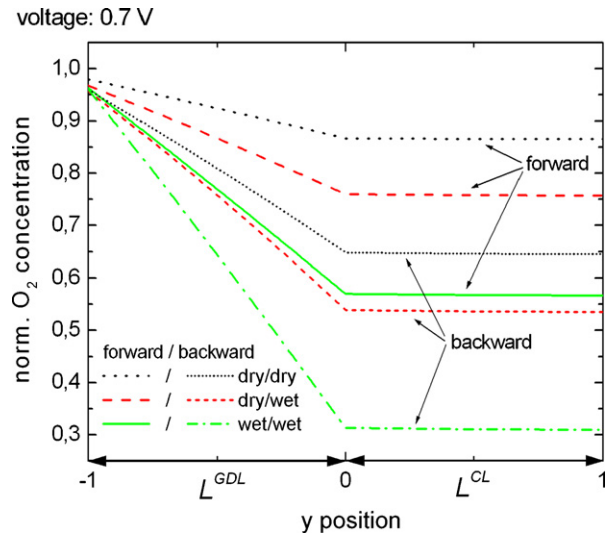
To the best of our knowledge, Shah et al. [39] are among the few using a Cauchy boundary condition, leading to a saturation of up to 0.6–0.8. Unlike in our model, they assume continuity of the saturation at the interface CL $\leftrightarrow$ GDL and therefore reached the maximum saturation level in the CL.

Fig. 12(a) shows the time-dependent system response in terms of current density and saturation at the interface GDL $\leftrightarrow$ channel for case (1). Both the maximum of current density ($\Delta\varphi_1$) and saturation ($\Delta\varphi_2$) display a phase shift relative to the minimum of the applied cell voltage. The cumulative saturation during the forward mode causes increasing mass transport limitation, which becomes the dominant loss mechanism in the high current density region. This in turn leads to a current density maximum which is considerably earlier than the voltage minimum (about 25 s). The saturation increases beyond this voltage minimum up to a phase shift of about $\Delta\varphi_2 = 90°$ (45 s). The evolution of the ionomer water content at the interface GDL $\leftrightarrow$ CL is analyzed in Fig. 12(b). The maximum of the water content shows only a small phase-shift relative to the voltage ($\Delta\varphi_3$), whereas the minimum of the water content shows a strong delay with respect to the voltage maximum ($\Delta\varphi_4$).

The evolution of the water content profile for case (2) is visualized in Fig. 13. In the region of maximum current density, labeled as (1), a water content of nearly 17 is reached in the CL. A strong gradient of the water content is observed in the y-direction due to the strong electro-osmotic drag at high current densities. The decreasing electro-osmotic drag during the backward sweep and the back diffusion leads to a balancing of the water content in the membrane (region (2)). In region (3), the introduced water from the humidified hydrogen stream at the anode and the water generation from the ORR in the cathode CL is insufficient to prevent dehydration of the ionomer. The water content falls to a value of 7.1.

4.4. Chronoamperometry

A comparison between measured and simulated chronoamperometry experiments is made in Figs. 14 and 15. The fuel cell was operated with dry air and humidified hydrogen ($T_{DP}^a = 311$ K) with the same flow rate as in the voltammetry experiments (see Table 1). The simulated voltage steps are corrected by the measured anode losses. Since the anode overvoltage shows small changes in time after a voltage step, the mean value is used. Overshoots in the
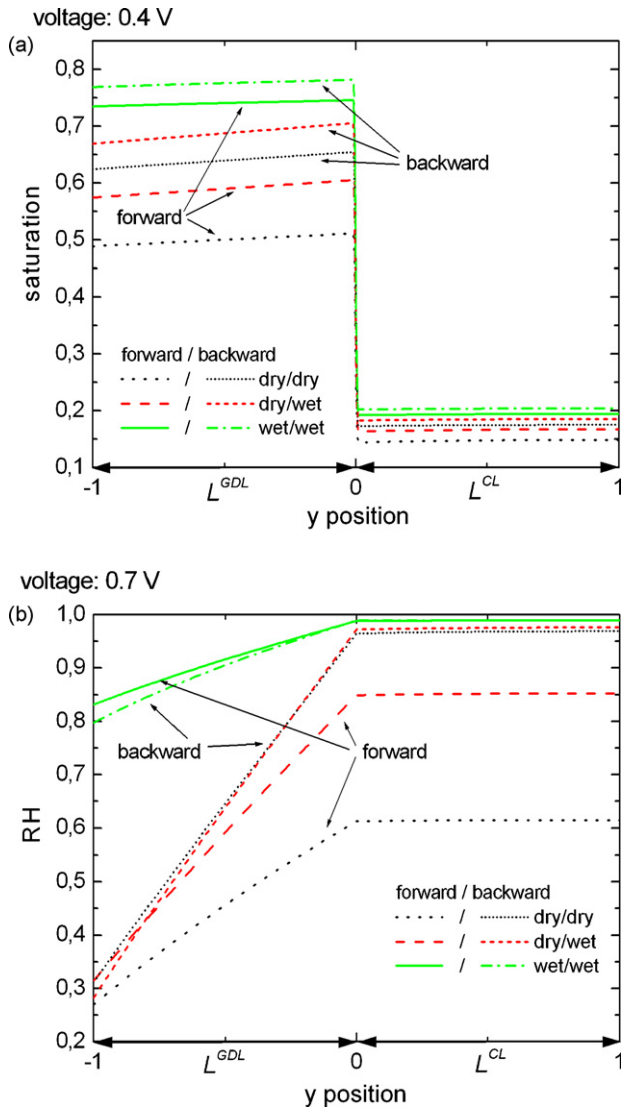
Fig. 11. Comparison of the profiles of the saturation (0.4 V) and the relative humidity (0.7 V) during a forward and a backward sweep. (a) Continuity in the capillary pressure at the interface results in a discontinuity in the saturation. A higher saturation is found in the backward mode. (b) The relative humidity (RH) for case (3) remains at nearly 100% during the entire sweep.

Fig. 12. The time-dependent characteristic of the applied cell voltage together with the system response in terms of cell current, saturation ($s[-1]$) and water content ($\lambda[0]$) is shown for case (1). (a) The maximum current density is reached about 20 s before the lowest cell voltage is reached ($\Delta\varphi_1$). The maximum saturation (interface channel ↔ GDL) has a delay ($\Delta\varphi_2$) of about 42 s relative to the minimum cell voltage. (b) The characteristic of the water content (interface GDL ↔ CL) follows that of the current density in principle. However, the decrease of the water content is a little delayed ($\Delta\varphi_4$) with respect to the cell current due to the liquid water reservoir in the catalyst layer.

measured current density are recorded on switching from high to low cell voltages (Fig. 14(a)). The characteristic of the overshoots depends on the voltage level before and after the step change. A change from 0.6 to 0.3 V (step (1)) causes a peak current density of 1.3 A cm^{-2} that drops off to a value of 0.9 A cm^{-2} within the first 20 s. The peak current density of step (2) reaches the same value but shows a less rapid decay than step (1). The peak in case (3) is not very pronounced, but shows an apparent delay relating to the step change, that is not observed for step (1) and (2) to this degree.

Switching from the low to the high cell voltage, the characteristic of the current response differs for all three steps. Step (1) shows an increase in the current density immediately after the voltage change and reaches equilibrium within 100 s. Step (2) shows a short increase or plateau before the current density starts to decrease. The current density in step (3) decreases continuously to a steady-state value.

The simulation shows a qualitatively similar characteristic (Fig. 14(b)). However, the time constants of the response differ from the measured ones. The simulation of steps (1) and (2) predicts a
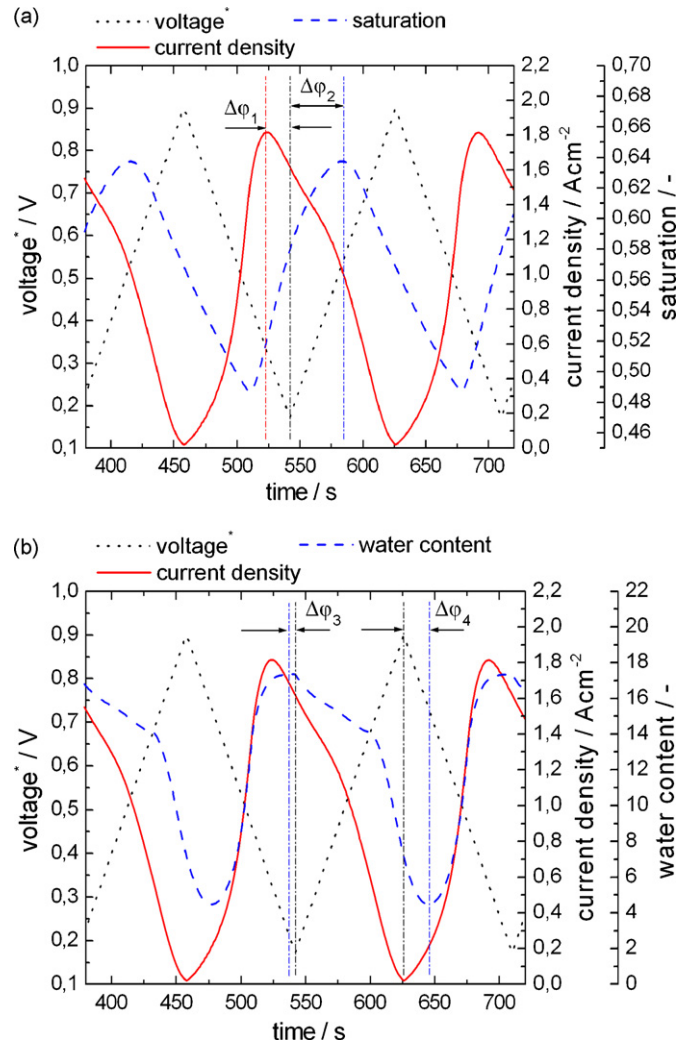
distinct overshoot in the current density with the same peak value of 1.5 A cm^{-2}. A sharp peak is observed for step (1), but step (2) shows a much slower decay than the measured data. Step (3) shows a linear decrease of the current without a clear peak. A delay of the maximum current relative to the step change is predicted by the model, in agreement with the measurement. The simulated current response to the potential step from low to high cell voltage is in agreement with the measurement. An increase of the current density for step (1), an increase in the current density followed by decrease for step (2) as well as the fast decay to a steady-state value for step (3) are predicted.

The corresponding cell impedance was recorded during the chronoamperometry measurements and is depicted in Fig. 15(a). Almost no change in the impedance was measured for step (1). The ionomer starts to dehydrate when the fuel cell is driven at a cell voltage of 700 mV (step (2)). Stepping back to 400 mV, the impedance drops very rapidly to a low impedance level, similar to the value of step (1). At a cell voltage of 800 mV, the impedance rises very fast
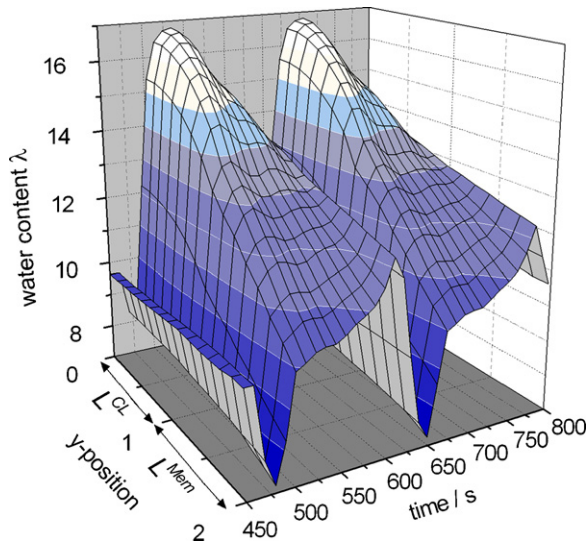
Fig. 13. The 3D diagram visualizes the evolution of the water content profile during two cycles of the sweep experiment for case (2). The water content is dominated by electro-osmotic drag and water generation (region 1), back diffusion (region 2) and dehydration (region 3).
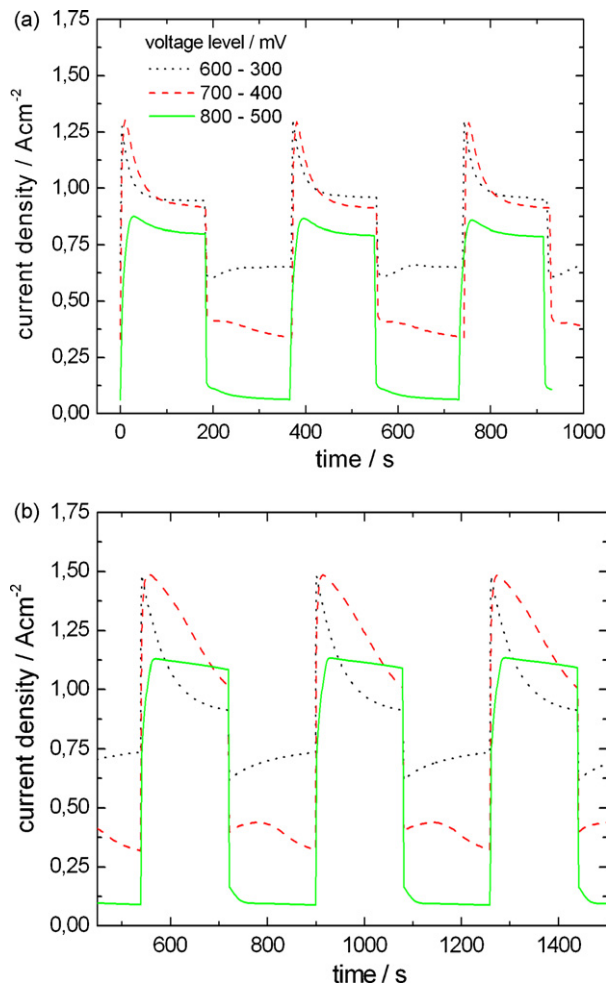

Fig. 14. Comparison between measured and simulated current response for chronoamperometry experiments. (a) An overshot is observed in all three cases on switching to the low cell voltage. The response differs on returning to the higher voltage, depending on the voltage level. (b) A qualitatively good agreement with the experiments was achieved in the simulations, but with a longer time constant.
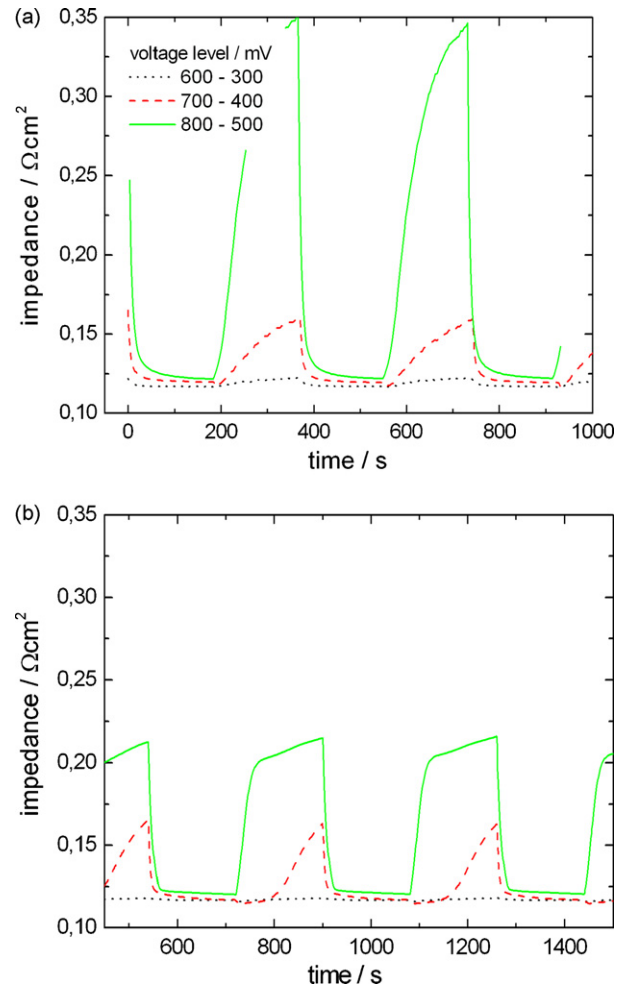
Fig. 15. Comparison between measured and simulated impedance responses during chronoamperometry experiments. (a) An increase in the impedance at cell voltages of 700 mV and above shows that the self-humidification by product water is insufficient. (b) The simulation predicts dehydration in the voltage range of 700 mV and above, but the simulated impedance is not as high as the measured impedance.

to a value of $0.35\,\Omega\,cm^2$ and drops again very fast on switching to higher current density and overvoltage.

The simulation of the impedance response describes the measured impedance qualitatively. While switching between 600–300 mV, dehydration of the ionomer can not be observed. In the range between 700–400 mV, the ionomer starts to dehydrate at a cell voltage of 700 mV. Strong dehydration of the ionomer at a cell voltage of 800 mV for step (3) is predicted by the model, but is obviously not as pronounced as in the measured data. A reason for this could be the shrinking of the ionomer in the case of high dehydration, resulting in an increase of the contact resistance that is not implemented in the model.

5. Conclusion

In PEM fuel cells, water is present as vapor, in liquid form and dissolved in the ionomer. The effects of water in all three phases, basically pore flooding and ionomer dehydration, are investigated with a newly developed 1D transient model. The model accounts for the loss mechanisms in the cathode GDL, cathode CL and membrane. The electrode structure is modeled as a network of spherical agglomerates. An excess of liquid water in the catalyst layer leads to coverage of these agglomerates, forming a water film which limits oxygen transport. Liquid water is

modeled as saturation in the void space. Its transport properties depend strongly on the capillary pressure–saturation relationship in porous media, which in turn is a function of the wettability and pore structure. Based on ESEM images, immobile saturation is introduced due to the observed partly hydrophilic regions in the GDL. We assume a continuous capillary pressure at the interface CL ↔ GDL, resulting in a discontinuous saturation distribution. Finite phase transition rates between the ionomer and pore space, namely adsorption/desorption and liquid water uptake/release, enable membrane dehydration in the case of dry operating conditions, resulting in an increased ohmic resistance.

The simulation results for dynamic current–voltage characteristics are in excellent agreement with our measured data. The measured hysteresis loop in the limiting current density region is reproduced by the model and explained by pore flooding. The measured cell impedance during a voltage sweep, which is a measure for the time-dependent water content, is in agreement with the simulation over a wide range of operating conditions and current densities. Simulations of chronoamperometry experiments are performed with the validated parameter set. The model captures qualitatively the current and impedance responses of measured chronoamperometry data.

Our model forms a suitable basis for identifying the dominant loss mechanisms at different operating points. Based on the simulation results, suggestions for a better choice of fuel cell components can be made, guidance for their physical properties like pore structure, wettability or thickness can be obtained or simply optimal operating conditions can be found. The latter leads us to the topic of fuel cell control. A good understanding of the response on dynamic load changes is required to control a fuel cell within a stable operating point. This can be realized by implementing our model in a simplified form in a model-based control algorithm.

Parameter studies and a sensitivity analysis would be the next steps in ongoing work. An upgrade to a multi-dimensional model is intended for the future.

6. Nomenclature and parameter list

Symbol	Description	Value / Eq.	Unit	Reference
Solving variables				
$c_{O_2}^g$	Normalized gaseous oxygen concentration		–	
c_v	Normalized vapor concentration		–	
s	Saturation		–	
T	Local temperature		K	
η	Overpotential		V	
λ	Water content		–	
Physical constants				
F	Faraday constant	96484	$C\,mol^{-1}$	
R	Gas constant	8.314	$J\,K^{-1}\,mol^{-1}$	
Structural values				
L^{CBP}	Thickness of cathode bipolar plate	3×10^{-3}	m	
L^{GDL}	GDL thickness	280×10^{-6}	m	
L^{CL}	CL thickness	10×10^{-6}	m	
L^{mem}	Membrane thickness	35×10^{-6}	m	
L^{ABP}	Thickness of anode bipolar plate	3×10^{-3}	m	
R_a	Mean agglomerate radius	0.2×10^{-6}	m	[57]
ϵ_a	Volume fraction of primary pores in an agglomerate	0.4	–	[26]
ϵ_p^{CL}	Volume fraction of secondary pores in CL	0.25	–	[40,22]
ϵ_i^{CL}	Volume fraction of ionomer in CL	0.3	–	
ϵ_p^{GDL}	Volume fraction of open pores in GDL	0.7	–	[58]
Λ	Agglomerate density	Eq. (23)	m^{-3}	
Ξ	Geometry factor	0.55	–	Calculated
Physical properties, local variables and boundary conditions				
a_w	Water activity	Eq. (30)	–	
$c_{O_2,s}^d$	Dissolved oxygen concentration at agglomerate surface	Eq. (3)	$mol\,m^{-3}$	
$\tilde{c}_{O_2}^d$	Normalized dissolved oxygen concentration in agglomerate	Eq. (2)	–	
$c_{O_2}^{g*}$	Gaseous oxygen concentration at inlet	Eq. (44)	$mol\,m^{-3}$	
c_v^*	Vapor concentration at inlet	Eq. (49)	$mol\,m^{-3}$	
C_{DL}	Double layer capacity	0	$F\,m^{-3}$	
$C_{Ti} = \rho_{Ti}\,c_{Ti}$	Heat capacity of titanium	9.4×10^6	$J\,m^{-3}\,K^{-1}$	[59]
$C^{GDL} = \rho_{GDL}\,c_{GDL}$	Heat capacity of GDL	1.61×10^6	$J\,m^{-3}\,K^{-1}$	[38]
$C^{CL} = \rho_{CL}\,c_{CL}$	Heat capacity of CL	1.61×10^6	$J\,m^{-3}\,K^{-1}$	[38]
$C^{mem} = \rho_{mem}\,c_{mem}$	Heat capacity of membrane	2.18×10^6	$J\,m^{-3}\,K^{-1}$	[38]
$C_g = \rho_g\,c_g$	Heat capacity of gas	1×10^3	$J\,m^{-3}\,K^{-1}$	[38]
$C_w = \rho_w\,c_w$	Heat capacity of water	4.187×10^6	$J\,m^{-3}\,K^{-1}$	[38]
d	Water film thickness	Eq. (17)	m	
$D_{O_2}^i$	Oxygen diffusion coefficient in ionomer	5×10^{-11}	$m^2\,s^{-1}$	[22]
$D_{O_2}^w$	Oxygen diffusion coefficient in water	2.1×10^{-9}	$m^2\,s^{-1}$	
$D_{O_2}^g$	Oxygen diffusion coefficient in gas phase	Eq. (46)	$m^2\,s^{-1}$	[42]
$D_{O_2}^{eff,\Omega}$	Effective oxygen diffusion coefficient in gas phase	Eq. (45)	$m^2\,s^{-1}$	[42]
D_v^g	Vapor diffusion coefficient in gas phase	Eq. (51)	$m^2\,s^{-1}$	
$D_v^{eff,\Omega}$	Effective vapor diffusion coefficient in gas phase	Eq. (51)	$m^2\,s^{-1}$	
D_s^Ω	Water diffusion coefficient in porous medium	Eq. (39)	$m^2\,s^{-1}$	
D_λ^i	Water diffusion coefficient in ionomer	Eq. (25)	$m^2\,s^{-1}$	[46]
EW	Equivalent weight	1.1	kg	[20]
h_{gl}	Heat of vaporisation/condensation	40.7×10^3	$J\,mol^{-1}$	[59]
H	Henry constant	0.0254	–	[41]

Symbol	Description	Value / Eq.	Unit	Reference
$j_{O_2}^g$	Gaseous oxygen flux	Eq. (43)	$\mathrm{mol\,m^{-2}\,s^{-1}}$	
j_v	Vapor flux	Eq. (48)	$\mathrm{mol\,m^{-2}\,s^{-1}}$	
j_s	Liquid water interstitial velocity	Eq. (34)	$\mathrm{m\,s^{-1}}$	
j_T	Heat flux	Eq. (53)	$\mathrm{J\,m^{-2}\,s^{-1}}$	
$j_{p,e}$	Charge flux	Eq. (19)	$\mathrm{A\,m^{-2}}$	
j_λ	Dissolved water flux	Eq. (24)	$\mathrm{mol\,m^{-2}\,s^{-1}}$	
j_{gen}^a	Current generation per agglomerate	Eq. (11)		
k_{ad}^a	Adsorption/desorption rate on anode	Eq. (71)	$\mathrm{s^{-1}}$	*Assumed*
k_{ads}	Adsorption rate	80	$\mathrm{s^{-1}}$	Assumed
k_{des}	Desorption rate	50	$\mathrm{s^{-1}}$	Assumed
k_{eva}	Evaporation rate	100	$\mathrm{m\,s\,kg^{-1}}$	[50]
k_{con}	Condensation rate	100	$\mathrm{s^{-1}}$	[50]
k_u	Water uptake rate	0.1	$\mathrm{mol\,s\,kg^{-1}\,m^{-2}}$	Assumed
k_r	Water release rate	0.1	$\mathrm{mol\,s\,kg^{-1}\,m^{-2}}$	Assumed
k_0	Reaction rate	0.001	$\mathrm{s^{-1}}$	Assumed
K_{abs}^{GDL}	Absolute permeability in GDL	8.7×10^{-12}	$\mathrm{m^2}$	[39]
K_{abs}^{CL}	Absolute permeability in CL	1×10^{-13}	$\mathrm{m^2}$	[39]
K_{rel}	Relative permeability	Eq. (40)		
n	Number of transfered electrons	2	–	
p_c^Ω	Capillary pressure in domain Ω		Pa	
p^{sat}	Saturation pressure	Eq. (31)	Pa	[1]
q_{ORR}	Source/sink term due to ORR	Eq. (22)	$\mathrm{A\,m^{-3}}$	
q_{ad}	Source/sink term due to adsorption/desorption	Eq. (28)	$\mathrm{mol\,m^{-3}\,s^{-1}}$	
q_{ur}	Source/sink term due to liquid water uptake/release	Eq. (33)	$\mathrm{mol\,m^{-3}\,s^{-1}}$	
q_{ec}	Source/sink term due to evaporation/condensation	Eq. (42)	$\mathrm{mol\,m^{-3}\,s^{-1}}$	
q_h	Source/sink term of the heat	Eqs. (55)–(59)	$\mathrm{J\,m^{-3}\,s^{-1}}$	
RH	Relative humidity	Eq. (30)	–	
$s_{im}^{GDL/CL}$	Immobile saturation	0.2/0	–	Assumed
α	Transfer coefficient	0.45	–	
α_{drag}	Electro-osmotic drag coefficient	Eq. (26)	–	
ΔS	Enthalpy change	162.2	$\mathrm{J\,mol^{-1}\,K^{-1}}$	[38]
Θ_m	Contact angle in ionomer channels	90.02	°	[36]
Θ^Ω	Contact angle in porous media (GDL/CL)	105/95	°	
κ_{GDL}	Thermal conductivity of GDL	1.67	$\mathrm{W\,m^{-1}\,K^{-1}}$	[38]
κ_{CL}	Thermal conductivity of CL	0.67	$\mathrm{W\,m^{-1}\,K^{-1}}$	[38]
κ_{mem}	Thermal conductivity of membrane	0.67	$\mathrm{W\,m^{-1}\,K^{-1}}$	[38]
κ_{Ti}	Thermal conductivity of titanium	21.9	$\mathrm{W\,m^{-1}\,K^{-1}}$	[59]
λ_{eq}	Equilibrated water content	Eq. (29)	–	[1]
μ	Liquid water viscosity	0.001	$\mathrm{kg\,m^{-1}\,s^{-1}}$	[2]
ν_g	Molar volume of ideal gas	2.2414×10^{-2}	$\mathrm{m^3\,mol^{-1}}$	
ν_w	Molar volume of liquid water	1.8015×10^{-5}	$\mathrm{m^3\,mol^{-1}}$	
ρ_i	Ionomer density	1980	$\mathrm{kg\,m^{-3}}$	[20,18]
σ_w	Surface tension of water	0.07		[2]
$\sigma_{contact}$	Unified conductivity of all electronic conductors normed to BP2	600/650	$\mathrm{S\,m^{-1}}$	Assumed
σ^Ω	Protonic conductivity in domain Ω	Eq. (20)	$\mathrm{S\,m^{-1}}$	[1]
$\Omega_{O_2}^c$	Oxygen transfer coefficient cathode	2.4×10^4	$\mathrm{m^{-2}}$	Assumed
Ω_v^c	Vapor transfer coefficient cathode	2.4×10^4	$\mathrm{m^{-2}}$	Assumed
Ω_s^c	Saturation transfer coefficient cathode	3×10^2	$\mathrm{m^{-2}}$	Assumed
Ω_w^a	Water transfer coefficient anode	1×10^{-5}	$\mathrm{m^{-2}}$	Assumed
Ω_T	Heat transfer coefficient	1150	$\mathrm{J\,K^{-1}\,m^{-2}\,s^{-1}}$	Assumed
Operating conditions				
i_{cell}	Current density		$\mathrm{A\,cm^{-2}}$	
p_{O_2}	Oxygen partial pressure	0.21	atm	
P	Total pressure	1	atm	
$T_{coolant}$	Coolant temperature	313	K	
T_{DP}^a	Anode dew point temperature	Various	K	
T_{DP}^c	Cathode dew point temperature	Various	K	
$\dot{V}_a$	Anode gas flow rate	50 (8.33×10^{-7})	$\mathrm{ml\,min^{-1}\,(m^3\,s^{-1})}$	
$\dot{V}_c$	Cathode gas flow rate	100 (16.66×10^{-7})	$\mathrm{ml\,min^{-1}\,(m^3\,s^{-1})}$	
U	Voltage		V	

References

[1] T.E. Springer, T.A. Zawodzinski, S. Gottesfeld, Journal of The Electrochemical Society 138 (8) (1991) 2334–2341.

[2] S. Mazumder, J.V. Cole, Journal of The Electrochemical Society 150 (11) (2003) A1510–A1517.

[3] T. Berning, N. Djilali, Journal of The Electrochemical Society 150 (12) (2003) A1589–A1598.

[4] U. Pasaogullari, C.Y. Wang, Electrochimica Acta 49 (2004) 4359–4369.

[5] M. Hu, A. Gu, M. Wang, X. Zhu, Energy Conversion and Management 45 (2004) 1861–1882.

[6] M. Hu, X. Zhu, M. Wang, A. Gu, L. Yu, Energy Conversion and Management 45 (2004) 1883–1916.

[7] J.J. Baschuk, X. Li, Journal of Power Sources 142 (2004) 134–153.

[8] U. Pasaogullari, C.Y. Wang, Journal of The Electrochemistry Society 151 (3) (2004) A399–A406.

[9] E. Birgersson, M. Noponen, M. Vynnycky, Journal of The Electrochemical Society 152 (5) (2005) A1021–A1034.

[10] U. Pasaogullari, C.Y. Wang, Journal of The Electrochemical Society 152 (2) (2005) A380–A390.

[11] H. Sun, H. Liu, L.J. Guo, Journal of Power Sources 143 (2005) 125–135.

[12] P. Berg, K. Promislow, J. St Pierre, J. Stumper, B. Wetton, Journal of The Electrochemical Society 151 (3) (2004) A341–A353.

[13] G. Lin, W. He, T.V. Nguyen, Journal of The Electrochemical Society 151 (12) (2004) A1999–A2006.

[14] H.K. Hsuen, Journal of Power Sources 137 (2004) 183–195.
[15] P. Berg, A. Novruzi, K. Promislow, Chemical Engineering Science 61 (2006) 4316–4331.
[16] A. Vorobev, O. Zikanov, T. Shamim, Journal of Power Sources 166 (2007) 92–103.
[17] H. Wu, P. Berg, X. Li, Journal of Power Sources 165 (2007) 232–243.
[18] Y. Wang, C.-Y. Wang, Electrochimica Acta 51 (2006) 3924–3933.
[19] W.-M. Yan, H.-S. Chu, J.-Y. Chen, C.-Y. Soong, F. Chen, Journal of Power Sources 162 (2006) 1147–1156.
[20] F. Chen, M.-H. Chang, C.-F. Fang, Journal of Power Sources 164 (2007) 649–658.
[21] M. Eikerling, Journal of The Electrochemical Society 153 (3) (2006) E58–E70.
[22] F. Jaouen, G. Lindbergh, G. Sundholm, Journal of The Electrochemical Society 149 (4) (2002) A437–A447.
[23] F. Jaouen, G. Lindbergh, Journal of The Electrochemical Society 150 (12) (2003) A1699–A1710.
[24] M.L. Perry, J. Newman, E.J. Cairns, Journal of The Electrochemical Society 145 (1) (1998) 5–15.
[25] D. Gerteisen, A. Hakenjos, J.O. Schumacher, Journal of Power Sources 173 (2007) 346–356.
[26] R. Madhusudana Rao, R. Rengaswamy, Journal of Power Sources 158 (2006) 110–123.
[27] D. Natarajan, T.V. Nguyen, Journal of The Electrochemical Society 148 (12) (2001) A1324–A1335.
[28] D. Natarajan, T.V. Nguyen, Journal of Power Sources 115 (2003) 66–80.
[29] N.P. Siegel, M.W. Ellis, D.J. Nelson, M.R. von Spakovsky, Journal of Power Sources 128 (2004) 173–184.
[30] K.S. Udell, International Journal of Heat and Mass Transfer 28 (1985) 485–495.
[31] M. Acosta, C. Merten, G. Eigenberger, H. Class, R. Helmig, B. Thoben, H. Mueller-Steinhagen, Journal of Power Sources 159 (2006) 1123–1141.
[32] E.C. Kumbur, K.V. Sharp, M.M. Mench, Journal of Power Sources 168 (2007) 356–368.
[33] J.H. Nam, M. Kaviany, International Journal of Heat and Mass Transfer 46 (2003) 4595–4611.
[34] C. Ziegler, H.M. Yu, J.O. Schumacher, Journal of The Electrochemical Society 152 (8) (2005) A1555–A1567.
[35] A.Z. Weber, J. Newmann, Journal of The Electrochemical Society 150 (7) (2003) A1008–A1015.
[36] A.Z. Weber, J. Newmann, Journal of The Electrochemical Society 151 (2) (2004) A311–A325.
[37] H.M. Yu, C. Ziegler, Journal of The Electrochemical Society 153 (3) (2006) A570–A575.
[38] A.A. Shah, G.-S. Kim, P.C. Sui, D. Harvey, Journal of Power Sources 163 (2007) 793–806.
[39] A.A. Shah, G.-S. Kim, W. Gervais, A. Young, K. Promislow, J. Li, S. Ye, Journal of Power Sources 160 (2006) 1251–1268.
[40] J. Ihonen, F. Jaouen, G. Lindbergh, A. Lundblad, Journal of The Electrochemical Society 149 (4) (2002) A448–A454.
[41] R. Sander, Compilation of Henry's Law Constants for Inorganic and Organic Species of Potential Importance in Environmental Chemistry, http://www.mpch-mainz.mpg.de/sander/res/henry.html, 1999.
[42] R.B. Bird, W.E. Stewart, E.N. Lightfoot, Transport Phenomena, 2nd edition, John Wiley and Sons, 2002.
[43] B. Andreaus, A.J. McEvoy, G.G. Scherer, Electrochimica Acta 47 (2002) 2223–2229.
[44] K.C. Neyerlin, H.A. Gasteiger, C.K. Mittelsteadt, J. Jorne, G. Wenbin, Journal of The Electrochemical Society 152 (6) (2005) A1073–A1080.
[45] E.W. Thiele, Industrial and Engineering Chemistry 31 (7) (1939) 916–920.
[46] Z. Liu, Z. Mao, C. Wang, Journal of Power Sources 158 (2006) 1229–1239.
[47] M.T. van Genuchten, Soil Science Society of America Journal 44 (1980) 892–898.
[48] R.H. Brooks, A.T. Corey, Hydrology Paper 3 (1964) 22–27.
[49] J. Bear, Dynamics of Fluids in Porous Media, Dover Publications, New York, 1972.
[50] W. He, J.S. Yi, T. Van Nguyen, AlChE Journal 46 (2000) 2053–2064.
[51] L. You, H. Liu, International Journal of Heat and Mass Transfer 45 (2002) 2277–2287.
[52] J.T. Gostick, M.W. Gowler, M.A. Ioannidid, M.D. Pritzker, Y.M. Volfkovich, A. Sakars, Journal of Power Sources 156 (2006) 375–387.
[53] T.E. Springer, T.A. Zawodzinski, M.S. Wilson, S. Gottesfeld, Journal of The Electrochemical Society 143 (2) (1996) 587–599.
[54] S. Um, C.-Y. Wang, Journal of Power Sources 156 (2006) 211–223.
[55] D. Gerteisen, Journal of Applied Electrochemistry 37 (2007) 1447–1454.
[56] Z.H. Wang, C.Y. Wang, K.S. Chen, Journal of Power Sources 94 (2001) 40–50.
[57] S. Litster, G. McLean, Journal of Power Sources 130 (2004) 61–76.
[58] P.K. Sinha, C.-Y. Wang, A. Su, International Journal of Hydrogen Energy 32 (2007) 886–894.
[59] VDI-Wärmeatlas Verein Deutscher Ingenieure, Springer-Verlag, Berlin/Heidelberg, 1988.